

AKARI Mission Program: Excavating Mass Loss History in Extended Dust Shells of Evolved Stars (MLHES) I. Far-IR Photometry*

Toshiya UETA¹, Andrew J. TORRES¹, Hideyuki IZUMIURA², Issei YAMAMURA^{3,4}, Satoshi TAKITA⁵ and Rachael L. TOMASINO¹

¹Department of Physics and Astronomy, University of Denver, 2112 E Wesley Ave., Denver, 80208, USA

²Okayama Branch Office, Subaru Telescope, NAOJ, NINS 3037-5 Honjo, Kamogata, Asakuchi, Okayama, 719-0232, JAPAN

³Institute of Space and Astronautical Science, JAXA, 3-1-1 Yoshinodai, Chuo-ku, Sagami-hara, Kanagawa, 252-5210, Japan

⁴Department of Space and Astronautical Science, SOKENDAI, 3-1-1 Yoshinodai, Chuo-ku, Sagami-hara, Kanagawa, 252-5210, Japan

⁵National Astronomical Observatory of Japan, 2-21-1 Osawa, Mitaka, Tokyo 181-8588, Japan

*E-mail: toshiya.ueta@du.edu

Received 2018 July 20; Accepted 2018 October 23

Abstract

We performed a far-IR imaging survey of the circumstellar dust shells of 144 evolved stars as a mission programme of the AKARI infrared astronomical satellite using the Far-Infrared Surveyor (FIS) instrument. With this survey, we deliver far-IR surface brightness distributions of roughly $10' \times 40'$ or $10' \times 20'$ areas of the sky around the target evolved stars in the four FIS bands at 65, 90, 140, and $160 \mu\text{m}$. Our objectives are to characterize the far-IR surface brightness distributions of the cold dust component in the circumstellar dust shells, from which we derive the amount of cold dust grains as low as 20 K and empirically establish the history of the early mass loss history. In this first installment of the series, we introduce the project and its aims, describe the observations, data reduction, and surface brightness correction process, and present the entire data set along with the results of integrated photometry measurements (i.e., the central source and circumstellar dust shell altogether). We find that (1) far-IR emission is detected from all but one object at the spatial resolution about $30'' - 50''$ in the corresponding bands, (2) roughly 60 – 70 % of the target sources show some extension, (3) previously unresolved nearby objects in the far-IR are now resolved around 28 target sources, (4) the results of photometry measurements are reasonable with respect to the entries in the AKARI/FIS Bright Source Catalogue, despite the fact that the targets are assumed to be point-sources when catalogue flux densities were computed, and (5) an IR two-color diagram would place the target sources in a roughly linear distribution that may correlate with the age of the circumstellar dust shell and can potentially be used to identify which targets are more extended than others.

Key words: surveys – circumstellar matter – stars: mass-loss – stars: AGB and post-AGB – infrared:

stars

1 Introduction

Low to intermediate initial mass stars (of $0.8\text{--}8 M_{\odot}$) experience copious mass loss at the rate of 10^{-8} to $10^{-4} M_{\odot} \text{yr}^{-1}$ in the late stages of evolution, especially during the asymptotic giant branch (AGB) phase (cf., Herwig 2005, Iben 2012, Karakas & Lattanzio 2014). This stellar mass loss is expected to be induced by specific physical conditions at the stellar surface as a consequence of the internal evolution, while the course of the internal evolution is thought to be influenced by this mass loss that impacts the physical conditions at the stellar surface. For example, mass loss may show temporal variations because of the alternative burning of hydrogen and helium in distinct layers via a mechanism called “thermal pulses” (Paczynski 1971) during the AGB phase, while a sudden, drastic increase of mass loss – the so-called “superwind” (Renzini 1981) – near the end of the AGB phase can remove a significant portion of the surface layer from the star, forcing the star to terminate the AGB evolution. The AGB mass loss, therefore, determines the fate of AGB stars by controlling the highest luminosity that they can attain and duration of the AGB phase, which would proportionally increase the lower limit of the zero-age main-sequence (ZAMS) mass that results in a supernova (c.f., Weidemann 1990). However, no theoretical description of mass loss has ever been derived fully from first principles, despite that identifying the exact mechanisms of mass loss in these cool stars has been and still is a long-standing problem in the stellar evolution.

During the AGB phase, mass-loss ejecta from the central star form a circumstellar dust shell (CDS)¹. When mass loss is terminated at the end of the AGB phase, the CDS becomes physically detached from the central star and starts to drift away. At this point, the newly-formed post-AGB CDSs appear to have already developed largely axisymmetric structures (cf., Meixner et al. 1999; Ueta et al. 2000; Meixner et al. 2002; Sahai et al. 2007; Siódmiak et al. 2008). Thus, the AGB mass loss affects not only the internal evolution but also the external evolution. While an ample amount of effort was made to confirm that the post-AGB CDSs do possess at least some axisymmetric structure, still lacking is the direct observational evidence

for the structure development in the AGB CDSs. In particular, the temporal evolution of the CDS structure development needs to be constrained by observations. Hence, a thorough observational study of the AGB CDSs must be done to understand the earlier AGB mass loss history pertaining to the CDS structure formation.

To follow the early AGB mass loss history observationally, one must employ far-IR thermal emission arising from the colder dust grains in the outermost regions of the CDSs as a primary tracer. While there is also molecular gas emission in the inner regions of the CDSs, molecules tend to be photo-dissociated by the interstellar radiation field (ISRF) in the outermost parts of the CDSs (e.g., Meixner et al. 1998). The presence of the ISRF does a favor for our purposes: (1) the ISRF would warm up dust grains in the outermost regions of the CDS at about $20\text{--}40\text{ K}$ (e.g., Gillett et al. 1986; Young et al. 1993a), and hence, would enhance, however slightly, the detectability of the CDSs in the far-IR, and (2) the CDSs are likely more extended than the molecular shells because of photo-dissociation by the ISRF, and possibly, by dust/gas drift. Thus, dust grains in these regions would not suffer from cooling by molecules.

Here, we present the far-IR imaging survey of evolved star CDSs at various evolutionary stages from the tip of the first giant branch to the planetary nebula (PN) phase including AGB and post-AGB phases, conducted using the AKARI infrared (IR) astronomical satellite and the Far-IR Surveyor (FIS) instrument. Our primary goals of this survey are to (1) detect far-IR emission from cold dust grains that reside in the CDSs of evolved stars, (2) perform photometry of the detected sources, and (3) establish the density distribution in the CDSs from the detected far-IR surface brightness distributions for the CDSs without the influence of the central star and reconstruct the AGB mass loss history in detail, and (3) quantify parameters concerning the AGB mass loss and CDS structures. In this first installment of the series, we introduce the project, describe the observations, data reduction, and surface brightness correction process, and present far-IR images for the entire sample of 144 targets along with the results of integrated photometry measurements made for the entire object (i.e., the central star and CDS altogether). Separation of the CDS and stellar emission via PSF removal and subsequent characterization of the CDS emission will be dealt with in the second installment of the series (Torres et al. *in preparation*).

¹ Indeed, a unique set of information, especially on the velocity and chemistry, of the mass-loss history can be derived from the gas component of the circumstellar gas shells (CGS). Readers who are also interested in following the latest developments in the investigation of the gas component of the AGB circumstellar shells are encouraged to refer to recent reviews such as the one by Höfner & Olofsson (2018).

2 Previous Far-IR Studies of the Evolved Star CDSs

The existence of very extended CDSs was originally recognized by individual spatial investigations by, for example, Hacking et al. (1985), Gillett et al. (1986), and Stencel et al. (1988), using IRAS (Neugebauer et al. 1984). Alternatively, Willems & de Jong (1988) and Chan & Kwok (1988) indicated the presence of the detached CDSs to explain the distribution of cool evolved stars on the IRAS 12-25-60 μm two-color diagram. Meanwhile, Young et al. (1993a) and Young et al. (1993b) were the first to fully exploit the potential of IRAS survey scan data in the far-IR, fitting the scan data passing over a target object by a simple CDS model. However, due to insufficient spatial resolutions, it was not possible to examine the internal structures of the extended CDSs around evolved stars until later when an advanced image processing technique was introduced (e.g., Waters et al. 1994; Izumiura et al. 1997; Hashimoto et al. 1998). Also, IRAS was not quite suited to probe the coldest dust emission from the evolved star CDSs as its reddest band was 100 μm . Then, ISO (Kessler et al. 1996) was used to observe a small sample (about 10) of evolved stars. Despite ISO's small sky coverage and large pixels, extended CDSs were detected and their structures were studied for both O-rich and C-rich AGB stars (e.g., Izumiura et al. 1996; Hashimoto & Izumiura 1998).

Although observations made with IRAS and ISO were successful, observational evidence was still lacking if we strive for the level of understanding that would allow more detailed characterization of mass loss and CDS structure formation during the AGB phase and beyond. In particular, detector sensitivities had to be improved to detect much weaker thermal dust emission, which may arise from a weakly mass-losing stars or the outermost regions of very extended CDSs. The former is necessary to learn mass loss experienced by lower progenitor-mass stars, while the latter is essential to investigate even earlier phases of mass loss.

At the turn of the 21st century, there was a *renaissance* of far-IR astronomy with the coming of the next generation of space telescopes launched successively – the Spitzer Space Telescope (Spitzer; Werner et al. 2004) in 2003 by the National Aeronautics and Space Administration, the AKARI IR astronomical satellite (AKARI; Murakami et al. 2007) in 2006 by the Institute of Space and Aeronautical Science (ISAS) of the Japan Aerospace Exploration Agency (JAXA), and the Herschel Space Observatory (Herschel; Pilbratt et al. 2010) in 2009 by the European Space Agency. These new opportunities

permitted us to probe CDSs at better sensitivities and spatial resolution than the preceding studies with IRAS and ISO.

However, observations of the extended CDS around evolved stars by Spitzer was met by a surprise. The bow-shock-like interface structure between the CDS and the interstellar medium (ISM) of $\sim 200''$ radius was detected in the far-IR around the AGB star, R Hya (Ueta et al. 2006), as part of the MIPS IR Imaging of AGB Dust shells (MIRIAD; PI: A. K. Speck) program. The detected structure was very much similar to the one found around Betelgeuse and other high-mass stars found earlier by IRAS, albeit smaller (Stencel et al. 1988; Noriega-Crespo et al. 1997). It was a surprise because the CDS-ISM interface structure was not expected around AGB stars, simply because the stellar wind velocity of AGB stars (of $10 - 20 \text{ km s}^{-1}$) was in general considered too low to cause shocks and active interactions at the CDS-ISM interface. As it turned out, what matters was the relative velocity of the stellar wind with respect to the local ISM. Hence, the CDS-ISM interactions can happen even for AGB stars if there is sufficient relative motion between the star and the local ISM (Ueta 2011). In fact, Herschel followed suit to discover the CDS-ISM interface structures in the far-IR in a significant fraction of the AGB stars and red supergiants in the sample (50 out of 78, or 63%; Cox et al. 2012) observed as part of the Mass-loss of Evolved StarS (MESS; PI: M. A. T. Groenewegen) guaranteed time key program (Groenewegen et al. 2011).

Meanwhile, a number of programs were executed to address the issue of AGB mass loss by probing the CDS density distributions in the far-IR, aiming to capture the onset of the axisymmetric structure development. Besides MIRIAD and MESS mentioned above, these programs include, COASTING (PI: M. Morris; Do et al. 2007), and Spitzer-MLHES (PI: T. Ueta; Ueta et al. 2010) with Spitzer, MLHES (PI: I. Yamamura; Ueta et al. 2007; Izumiura et al. 2009), and FISPIN (PI: P. Garca-Lario; Cox et al. 2011) with AKARI, and HerPlaNS (Herschel Planetary Nebula Survey; PI: T. Ueta; Ueta et al. 2017; Otsuka et al. 2017) with Herschel.

Unfortunately, mapping extended CDSs with Spitzer turned out to be challenging because (1) a significant portion of the MIPS 70 and 160 μm arrays were lost during launch and (2) the central star had to be avoided to prevent the MIPS 24 μm array from saturating (even when the 24 μm data were not needed). Nevertheless, both of the MIRIAD and Spitzer-MLHES programs yielded a certain amount of results: besides the R Hya discovery of the CDS-ISM interface (Ueta et al. 2006), another peculiar CDS-ISM interface case of R Cas was studied (Ueta et al.

2010). However, because Spitzer CDS maps usually lack the central $50'' \times 100''$ region, the latest mass loss history cannot be learned effectively from these maps.

The MESS program was a major survey of the evolved star CDSs with Herschel. The power of its unprecedented spatial resolution was seen from the detection of wakes due to instabilities in the CDS-ISM interface structures around X Her and TX Psc (Jorissen et al. 2011) and the CDS-ISM interface structure around Betelgeuse resolved into three separate arcs (Decin et al. 2012), besides the discovery of a number of CDS-ISM interaction cases (Cox et al. 2012). As for more genuine CDS cases, Kerschbaum et al. (2010) detected a detached circular CDS almost coincident with the previously known CO circular shell around AQ And, U Ant, and TT Cyg. Moreover, following the discovery of the spiral structures due to mass loss modulations of the central binary system in CO (Maercker et al. 2012), Mayer et al. (2013); Mayer et al. (2014) found internal spiral structures in the far-IR CDS characteristic to mass loss modulations of the central binary system.

Some of the AKARI maps were also already presented in the context of the CDS-ISM interface structure (Ueta et al. 2008; Ueta et al. 2010). Izumiura et al. (2011) revealed a detached CDS after removing the point-spread function (PSF) effects due to the central star by subtracting a scaled image of a reference point source and interpreted the deduced radial profiles as caused by (1) the temporal enhancement of mass loss due to thermal pulse and the subsequent two-wind interactions or (2) the reverse/termination shock of the stellar wind bounced back from the CDS-ISM interface. While the former scenario was likely and preferred, the latter scenario was not completely refuted by the presence of the cometary tail structure seen (Fig. 8 in Izumiura et al. 2011) and the marginal image quality at the preliminary stage of the data reduction.

3 Observations

3.1 AKARI Infrared Astronomical Satellite

AKARI (formerly ASTRO-F) was the Japanese IR space mission launched on 2006 February 21 (UT). The mission goals of AKARI are to (1) perform a high spatial resolution all-sky survey in six IR bands from 9 to $160 \mu\text{m}$, and (2) conduct pointed observations of specific targets to obtain deeper images and spectroscopic data from 2 to $180 \mu\text{m}$. AKARI carried out its 550-day cryogenic mission until it exhausted its liquid helium on 2007 August 26, and continued its post-cryogenic mission in the near-IR until the satellite was finally turned off on 2011 November 24.

The Far-IR Surveyor (FIS: Kawada et al. 2007) was one of the two instruments on-board AKARI, covering the wavelength range of 50 to $180 \mu\text{m}$ with two sets of Ge:Ga arrays, the Short Wavelength (SW) detector in the N60 ($50\text{--}80 \mu\text{m}$, the reference wavelength $\lambda_{\text{ref}} = 65 \mu\text{m}$) and WIDE-S ($60\text{--}110 \mu\text{m}$, $\lambda_{\text{ref}} = 90 \mu\text{m}$) bands (Fujiwara et al. 2003) and the Long Wavelength (LW) detector in the WIDE-L ($110\text{--}180 \mu\text{m}$, $\lambda_{\text{ref}} = 140 \mu\text{m}$) and N160 ($140\text{--}180 \mu\text{m}$, $\lambda_{\text{ref}} = 160 \mu\text{m}$) bands (Doi et al. 2002). During all-sky survey observations, the sky was swept at 3.6 s^{-1} covering more than 98% of the entire sky (the all-sky scan mode; Doi et al. 2015; Takita et al. 2015). During pointed observations, on the other hand, intended targets were scanned about $\times 20$ slower at 8 or $15'' \text{ s}^{-1}$ to achieve one to two orders of magnitude better sensitivity than the all-sky survey observations (the slow-scan mode; Shirahata et al. 2009).

As we will demonstrate below, AKARI slow-scan maps achieve the $1\text{-}\sigma$ sensitivity of less than 1 MJy sr^{-1} , thanks to the slow scan-mapping speed, its cooled mirror, and the marginal spatial resolution (as opposed to Herschel maps that went as deep as $\gtrsim 1 \text{ MJy sr}^{-1}$ $1\text{-}\sigma$ sensitivities; cf. Groenewegen et al. 2011; Ueta et al. 2014). Hence, AKARI CDS maps are by far the most sensitive far-IR images of evolved star CDSs ever produced.

3.2 Observing Strategy

Our primary aim is to establish the AGB mass loss history observationally to enhance our understanding of mass loss and the CDS structure formation. To trace the history of AGB mass loss over the last 10^5 years, it is necessary to examine the CDS out to 1.5 pc from the central star assuming the shell expansion velocity of 15 km s^{-1} . This means that the apparent size of the CDSs is on the order of $100''$ at typical distances of evolved stars ($\sim 1 \text{ kpc}$). Meanwhile, we also need to cover the sufficient amount of blank sky to assure reliable background subtraction for the clear detection of CDSs. Furthermore, we must examine the CDS structures in 2-D maps to distinguish between a real extension of dust emission and a local cirrus that mimics a dust shell in a 1-D scan. 2-D mapping is also important to study non-spherical morphologies expected in the CDSs around AGB and post-AGB stars. Therefore, the use of 2-D mapping in our investigation is essential, and thus, we employ the Astronomical Observation Template (AOT) FIS01, which is designed for photometry observations of compact sources in the slow-scan mode, to make scan maps of $10' \times 20'$ (width \times length) typically in the SW bands.

This AOT performs two round-trip scans along the in-

scan direction in the vicinity of the target source during the ~ 10 min window of pointed observation in the 90-min sun-synchronous orbit. Between two round-trip scans, there is a small offset along the cross-scan direction to secure coverage of the target source by different detector elements. In the end, this AOT provides four independent redundant scans of the target to be combined into a single map, assuring the reliability of the resulting map. For the actual execution of the AOT, we use a reset interval of 0.5, 1.0, or 2.0 sec, the scan speed of 8 or $15'' \text{ s}^{-1}$, and the cross-scan offset of 70 or $240''$ depending on the expected surface brightness and size of the target.

3.3 Target Selection

Our understanding of mass loss and the CDS structure formation can only be enhanced by collecting data from a large number of sources at various evolutionary stages (i.e., at the AGB, post-AGB/proto-PN, and PN phases), of different pulsation types (i.e., of Lb, SR, and Mira), and of different chemical types (i.e., C-, M-, and S-type). For the AKARI MLHES mission program, we establish first a volume limited sample of evolved stars before the launch of AKARI by the following procedure:

AGB stars 1) we extract known Lb, SR(a,b,c), and Mira type variables from the IRAS point source catalog, 2) we calculate the bolometric flux for each source using the $12 \mu\text{m}$ flux density and a bolometric correction based on the mid-IR color by $\log(F_{25}/F_{12})$, 3) we estimate the distance to these sources by assuming a bolometric luminosity of $2,500 L_{\odot}$ for all sources and extract those closer than 500 pc. Note that the luminosity is set conservatively somewhat smaller than the average value of $3,000 L_{\odot}$ for AGB stars (e.g., $2,600 L_{\odot}$ by Habing et al. 1985; $3,000 L_{\odot}$ by Knauer et al. 2001; $3,500 L_{\odot}$ by Jackson et al. 2002).

OH/IR stars 1) we extract IRAS point sources which have mid-IR colors typical for OH/IR stars, 2) we calculate the bolometric flux for each source using the $12 \mu\text{m}$ flux density and a bolometric correction based on the mid-IR color, 3) we estimate the distance to these sources by assuming a bolometric luminosity of $5,500 L_{\odot}$ for all sources and extract those closer than 1,000 pc. Note that the distance limit for OH/IR stars is larger because the space density of OH/IR stars is very low and we do not find any of them within 500 pc.

Post-AGB stars/Proto-PNe 1) we examine literature for known post-AGB candidates (e.g., Szczerba et al. 2007), 2) we extract sources which were found to

be extended in the far-IR (e.g., Speck et al. 2000).

PNe 1) we extract known PNe in the IRAS point source catalog (e.g., Acker et al. 1992), 2) we select those with galactic latitude greater than 20° , 3) we extract those that are bright in the IR using the Innsbruck Data Base of Galactic Planetary Nebulae (Kimeswenger & Kienel 1997).

Extended Sources We also include evolved objects which were previously found to be extended in the IRAS/ISO far-IR bands in the literature.

We then check the AKARI visibility of the selected targets and exclude those with low visibilities. Among the resulting sample, we give the highest priority to those that (1) show extension in the previous IRAS survey scan data (e.g., Young et al. 1993a; Young et al. 1993b), (2) are reported to possess an extended CDS in the ISO studies (e.g., Izumiura et al. 1996; Hashimoto & Izumiura 1998), and (3) are found to be extended in our unpublished studies using the High Resolution IRAS images and ADDSCAN data. We also take into account the critical observing conditions/constraints such as saturation, sensitivity, map size, and detection reliability. Sources located in high far-IR background regions are removed from the target list: we set the limiting threshold as 20 MJy sr^{-1} at $100 \mu\text{m}$. However, the last criterion greatly reduces the number of promising candidates. Last but not least, the target size is practically limited by the fact that we are awarded with 150 pointings, of course.

3.4 Observations

The science operation of AKARI, consisting of large-area survey programs (LSs), mission programs (MPs), and open-time programs (OTs), began on 2006 May 8. The all-sky survey was prioritised during Phase 1, which lasted until 2006 November 10. In addition to the all-sky survey, surveys of the North Ecliptic Pole and Large Magellanic Cloud were conducted as the LS program. Most of the MPs and OTs, including our observations, were executed during Phase 2, which followed Phase 1 and continued until the end of AKARI's cold campaign. In the end, 149 pointed observations are made by AKARI under the MLHES MP between 2006 September 9 and 2007 August 20, of which 144 are FIS scans in the far-IR and five are IRC mapping in the mid-IR. Some of the IRC maps have already been presented (Arimatsu et al. 2011). Table 1 summarizes the 144 FIS targets and their basic characteristics, together with a log of observations including target name (usually the target's IRAS designation), alternative/more common name, equatorial coordinates (J2000), Simbad object type, variability type, spectral type, date of observations, time of

observations, observation ID (a unique number to specify an AKARI data set), and AOT parameters.

4 Data Reduction

The AKARI/FIS slow-scan mapping data are archived in the Data ARchives and Transmission System (DARTS) maintained by ISAS/JAXA² in the time-series data (TSD) format. After the archived TSD sets are downloaded from DARTS, they need to be processed into co-added far-IR maps with a map-making tool. We employ the second-generation data reduction package, FIS AKARI Slow-scan Tool (FAST: Ikeda 2012; also briefly described by Ueta et al. 2017). While FAST is similar to the first-generation data reduction package, FIS Slow-Scan data analysis Toolkit (SS-Tool: Matsuura et al. 2007), FAST can perform superior glitch and calibration lamp after-effect removal (Suzuki et al. 2008).

During the AOT FIS01 scan sequence in orbit, calibration measurements are taken five times before and after each of the four parallel scan legs with the shutter closed (Kawada et al. 2007). The dark current and calibration lamp signals are monitored during each of these five calibration exposures to follow the time-varying instrument responsivity. On the other hand, self flat-field measurements, in which a flat frame is constructed to correct for the pixel-to-pixel detector responsivity variations, are made with the shutter opened by exposing the detector to the “flat” sky during the calibration sequences at the beginning and end of the entire scan sequence (pre-cal and post-cal) while the telescope transitions between the all-sky survey mode and the slow-scan pointed observation mode (Matsuura et al. 2007).

While SS-Tool is set to use all of the dark subtraction, detector responsivity time variation correction, and the pre-cal flat-fielding, FAST allows users to determine whether or not particular calibration measurements are used in the data processing with the help of the GUI, which visualizes the calibration measurements in the TSD. This flexible selection of calibration measurements with FAST greatly enhances the effectiveness of the corrections and improves the resulting data quality. This is especially true because it is now possible to discard calibration data that are compromised by anomalies. These improvements available in FAST results in cleaner final co-added maps than those made by SS-Tool.

Yet another difference between SS-Tool and FAST is how photon energy is assumed to be distributed over the FIS arrays for each photon hit in respective map-making

processes. With SS-Tool, photon energy is always distributed uniformly within the pre-determined beam size (i.e., a boxcar/pillbox function) of 40'' and 60'' for the SW and LW band, respectively. With FAST, however, a variety of gridding convolution functions such as Gaussian and sinc functions are available to users (Ikeda 2012). For the present work, we opt to adopt a Gaussian gridding convolution function (GCF) that would mimic the Airy disk of 33'' and 51'' at 90 and 140 μm , respectively. These parameters are chosen because they would reproduce the diffraction limit at the respective wavelengths in the resulting maps. Our particular parameter choices are different from those made by Ueta et al. (2017), and therefore, would inevitably result in slightly different PSF shapes. Hence, we need to derive our own surface brightness correction factors (see the next section; also see Appendix 1).

We thus take advantage of the improved capability of FAST to optimize calibration and angular resolution of the resulting co-added maps. In the final map-making, we orient the resulting images to align with the scan direction (i.e., the image y -direction is parallel to the scan direction; also see Figure 3 of Kawada et al. 2007) and use the following options: Earth-shine/stray-light removal, 200 s median filtering, 5- σ clipping, and GCF corresponding to the Airy disk of 33'' and 51'' at 90 and 140 μm . The resulting FAST co-added maps are produced at the pixel scale of 8'' pix^{-1} (corresponding to roughly 1/4 to 1/6 of the angular resolution).

5 Surface Brightness Correction

The absolute surface brightness calibration of the FIS instrument was done through (1) pre-launch laboratory measurements of a blackbody source which indicated a 5% accuracy, and (2) in-orbit comparisons between measurements of IR cirrus regions without significant small-scale structures made by FIS and the DIRBE instrument on board the COBE satellite (Matsuura et al. 2011). Hence, the FIS data (both all-sky and slow-scan data) presently archived should give correct surface brightnesses of diffuse background emission. However, when aperture photometry was performed for a set of IR flux standard stars detected in the COBE/DIRBE-calibrated FIS slow-scan maps (processed by SS-Tool), the resulting fluxes came out to be roughly 40% less than expected (Shirahata et al. 2009). This apparent flux underestimates were attributed to the slow transient response of the Ge:Ga detectors (e.g., Kaneda et al. 2002).

To alleviate this issue, Shirahata et al. (2009) devised a method of flux correction for point sources detected in the AKARI/FIS slow-scan maps processed by SS-Tool. This

² <http://darts.isas.jaxa.jp/astro/akari/>

point-source flux correction method is based on the premise that the shape of the PSF is well-defined and invariant with the source flux. This point-source flux correction method works because flux within an idealized infinite aperture can always be recovered by scaling the flux measured within a finite aperture (which corresponds to a part of the bright PSF core) by an appropriate aperture correction factor. However, such a correction method would not work in general for objects that are neither point-like nor diffuse (i.e., marginally extended, such as CDSs), because the surface brightness distribution of such an object is not known *a priori* (and hence the aperture correction factor cannot be uniquely determined).

Ueta et al. (2017) established a general procedure to correct directly the far-IR surface brightness distribution of AKARI/FIS slow-scan maps generated by SS-Tool or FAST. This procedure is based on the empirical power-law FIS detector response function, \mathcal{R} , which is defined to be

$$S_{ij,\text{FIS}} = \mathcal{R}(S_{ij}) = cS_{ij}^n, \quad (1)$$

where $S_{ij,\text{FIS}}$ is the measured surface brightness distribution in the archived, uncorrected FIS map, S_{ij} is the “true” surface brightness distribution of the mapped region of the sky in the far-IR, n and c are, respectively, the power-law index and the scaling coefficient of the adopted power-law FIS response function, and i and j refer to the pixel position in the FIS map.

This FIS response function was determined to possess a power-law form given the observed scale-invariant characteristics of slow-scan maps (i.e., PSF shapes remain the same irrespective of the PSF brightness). With this formulation, one can recover the true far-IR surface brightness distribution of the sky falling onto the FIS detectors via the inverse function, \mathcal{R}^{-1} , via

$$S_{ij} = \mathcal{R}^{-1}(S_{ij,\text{FIS}}) = (S_{ij,\text{FIS}}/c)^{1/n}. \quad (2)$$

with the appropriately-determined n and c power-law scaling parameters. The n and c parameters adopted in the present work are listed in Table 2. These parameters are slightly different from those previously determined by Ueta et al. (2017), because, as stated in the previous section, we opt to adopt specific GCF parameters to optimize the resulting PSF shape. The derivation of the present n and c values is outlined in Appendix 1 in detail. The resulting surface-brightness-corrected AKARI/FIS maps of the MLHES target sources are exhibited in Figure 1 and Supplementary Figures 1 through 28³.

³ Supplementary Figures 1 through 28 are available only in the on-line version.

6 Photometry

After AKARI/FIS maps of the MLHES target sources are processed and their surface brightnesses are corrected as described in the previous sections, we measure the total flux density for each target source in each of the four AKARI/FIS band using the following three-step procedure, scripted with Python aided by the Astropy package.

Step 1: We determine the first-pass sky surface brightness, I_{sky} , and its uncertainty, σ_{sky} , by taking the median and standard deviation of the entire FIS map, respectively, using 3- σ clipping. We then define the extent of the target source by adopting a region-growth algorithm. With this algorithm, a given region starting with the seed pixel at the target coordinates is grown by finding and incorporating all pixels that are connected neighbors to the region pixels as long as their pixel surface brightness value registers greater than the tentative sky value by $2\sigma_{\text{sky}}$ or more (i.e., $\geq (I_{\text{sky}} + 2\sigma_{\text{sky}})$).

Step 2: We then establish the sky regions adjacent to the grown target region in the surface brightness map (i.e., fore and aft directions along the scan path) to determine the second-pass I_{sky} and σ_{sky} by taking the median and standard deviation of the pixels within the sky regions using 3- σ clipping. With the re-determined I_{sky} and σ_{sky} , we use the region-growth algorithm again to re-define the extent of the target source. The source region is grown to include all connected pixels registering greater than the updated sky value by $2\sigma_{\text{sky}}$ or more. The adopted $2\sigma_{\text{sky}}$ threshold is chosen from comparisons among 1, 1.5, 2, 2.5, and $3\sigma_{\text{sky}}$ to find the optimum level that would recover the faintest surface brightness of the target sources while not including spurious emission from the sky or nearby sources.

This iteration is intended to make sure that the extent of the target source comes as low in the surface brightness as possible and that the sky regions do not overlap with the derived extent of target source. For this region-grow method to work, however, the target sources are assumed to have a single emission peak at the target position with their surface brightness distributions in general radially decreasing monotonically. This assumption, however, is not always true because the surface brightness distribution can vary considerably when the circumstellar shell possesses noticeable structures. Thus, we also visually inspect the results of the second-pass region-grow algorithm to check especially if real structures are missed or spurious structures are included. There are indeed cases where (1) what appears to be a nearby source is present in the immediate vicinity of the target (e.g., I00042⁴, I00245, I04020,

⁴ From here, we refer to our targets by the abbreviated IRAS designation, an

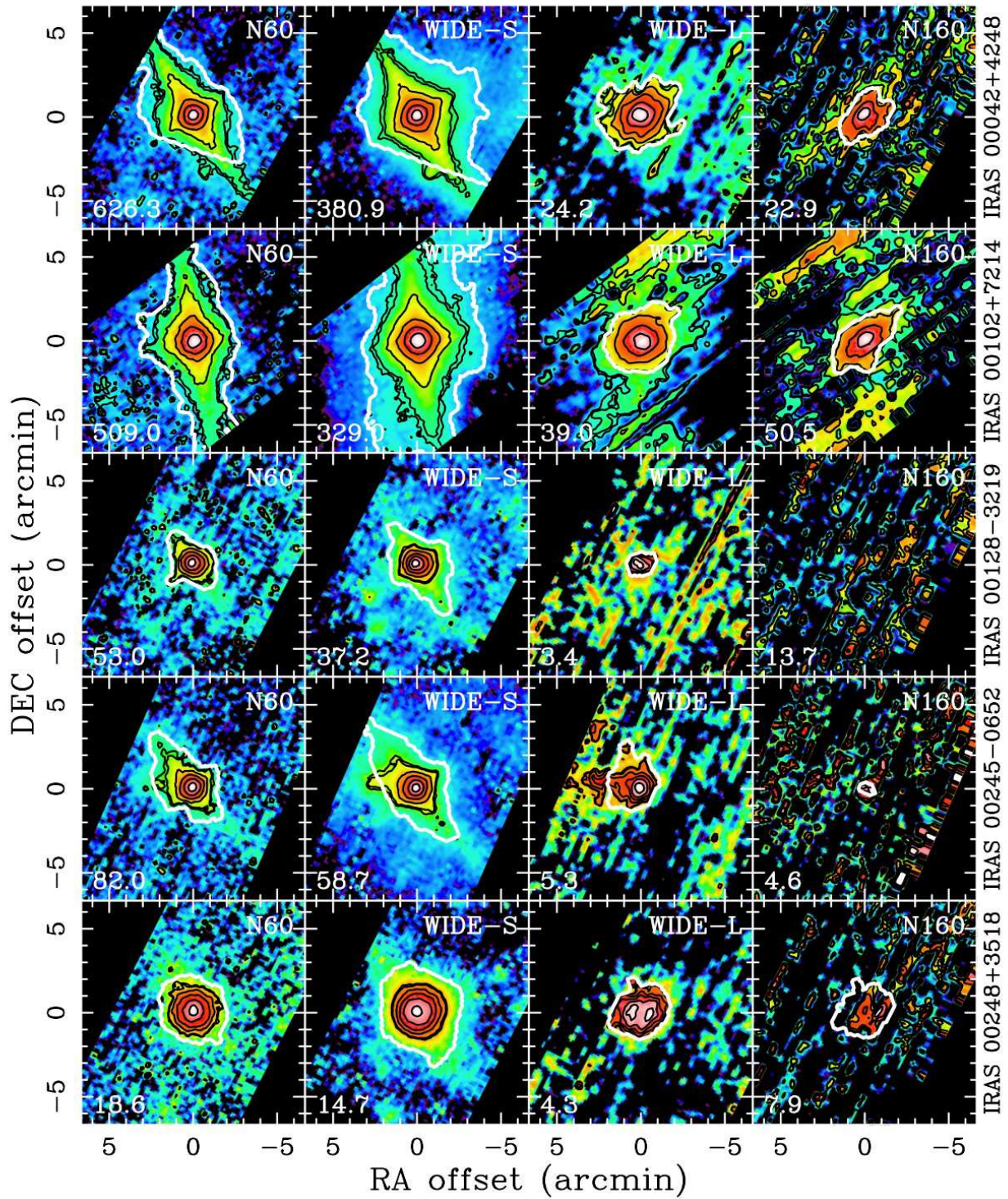


Fig. 1. Grayscale far-IR images of the MLHES target sources in the four AKARI/FIS bands (N60, WIDE-S, WIDE-L, and N160) from left to right, respectively. Each panel shows a $13'3 \times 13'3$ region centered at the RA-DEC coordinates of the target, whose name is shown on the right margin. White contours are 90, 70, 50, 30, 10, and 5% of the peak surface brightness, which is given on the bottom left corner of each frame. The black contour represents the adopted photometry boundary at each band.

I16011, I21197, I21440, and I27173), and (2) the target object is confused by the strong large-scale background emission (e.g., I3062 and I21419). These cases are handled on an individual basis by manually modifying the photometry boundary to exclude confused parts. In general, nearby sources are deemed real when they appear in more than one consecutive bands and/or exhibit different emission characteristics than the target source itself (i.e., the way the brightness varies across bands is dissimilar).

Also, there are cases where the background is too noisy to define a reasonable boundary at the adopted $2\sigma_{\text{sky}}$ threshold. In such cases, the target sources may not be automatically recognized even though they may appear obvious to human eyes. If that is the case, we adopt the boundary determined at the waveband of the best data quality (typically the waveband of the shortest wavelength where the boundary was algorithmically determined; i.e., the WIDE-L boundary is adopted for the N160 band, and the WIDE-S boundary is adopted for the WIDE-L and N160 bands). At any rate, whenever we adopt the photometry boundary that is not algorithmically determined (i.e., there is some manual intervention), it is noted in Table 3. These manual modifications of the photometry boundary typically introduce a difference of at most a few % (nearby source cases) to a few tens of % (background confusion cases).

Step 3: We then compute the flux density of the target source and its uncertainty using the following formulae:

$$F_\nu = \sum_{i,j}^{\text{obj}} \text{img}(i,j) - \frac{N_{\text{obj}}}{N_{\text{sky}}} \sum_{i,j}^{\text{sky}} \text{img}(i,j) \quad (3)$$

$$\sigma_{F_\nu}^2 = \sum_{i,j}^{\text{obj}} \text{err}(i,j)^2 - \frac{N_{\text{obj}}}{N_{\text{sky}}} \sum_{i,j}^{\text{sky}} \text{err}(i,j)^2 + N_{\text{obj}} \sigma_{\text{sky}}^2 + \frac{N_{\text{obj}}^2}{N_{\text{sky}}} \sigma_{\text{sky}}^2 \quad (4)$$

where $\text{img}(i,j)$ is the re-calibrated surface brightness map and $\text{err}(i,j)$ is the associated uncertainty map, N_{obj} and N_{sky} are the number of pixels within the extent of the target object (“obj”) and of the corresponding sky region (“sky”), respectively, and σ_{sky} is the standard deviation in the sky regions. The second-pass sky regions immediately before and after the second-pass grown target source region are referred to as the sky regions (“sky”), while the second-pass grown target source region itself is referred to as the target object region (“obj”). Similarly, the corresponding regions in the associated error map are referred to as in the same way (as the “sky” and “obj”), respectively. The $\text{err}(i,j)$ term corresponds solely to the uncertainties of the

detector signal per sampling, while σ_{sky} is the fluctuation of the observed sky emission (i.e., confusion noise and uncertainties of the detector signal per sampling): the σ_{sky} term is often a significant component in the far-IR.

The second term of eqn (3) subtracts the sky contribution in the target area. The first term in eqn (4) is a mixture of the photon shot noise due to signals from the target, photon shot noise due to sky emission, readout noise, dark current noise, and uncertainties in flatfielding. The third term in eqn (4) refers to the uncertainty that arises in the target region due to sky fluctuation (i.e., the photon shot noise due to sky emission, confusion noise, readout noise, dark current noise, and uncertainties in flatfielding, assuming that similar sky fluctuation continues into the target region). Finally, the fourth term in eqn (4) is the uncertainty due to sky subtraction. Thus, we are actually double-counting the photon shot noise due to sky emission, readout noise, dark current noise, and uncertainties in flatfielding. Hence, the second term in eqn (4) is included to compensate for those doubly-added noise terms. In addition, surface brightnesses of the re-calibrated map and its associated uncertainty map are converted from the native MJyr⁻¹ to Jy pix⁻¹ units given the adopted pixel scale at 8'' pix⁻¹ to yield flux densities in the end.

The measured flux densities of the MLHES target sources in the four AKARI far-IR bands are presented in Table 3. The listed flux densities are expressed in scientific notation, $a \pm b(c)$, where $a \pm b$ is the absolute value and c is the power index of base ten, i.e., $(a \pm b) \times 10^c$. Here, readers are reminded that these flux densities are the sum of the flux densities from the central star and the CDS. In this list, we also note if the photometry aperture boundary set by the procedure outlined above is manually adjusted (e.g., a nearby object needs to be removed) or adopted from a shorter waveband (e.g., the sky is too noisy to define a decent aperture in the present band).

In addition, we also present the far-IR sky surface brightnesses and their uncertainties at the positions of the MLHES target sources (Table 4). These sky values are computed by taking the median and standard deviation of the sky-only maps, which are created by taking the difference between the surface-brightness-corrected FIS maps with the median-filter on (i.e., the sky emission is subtracted from the map) and off (i.e., the sky emission remains in the map).

“l” followed by the first 5 digits of the IRAS designation, or alternative name when there is no IRAS designation.

7 Discussion

7.1 AKARI/FIS Images of Evolved Star CDSs

One of the main objectives of the present investigation is to understand the history of AGB mass loss via the far-IR surface brightness distribution of the cold dust component in the evolved star CDSs. This is because the CDSs are the direct consequences of mass loss. Upon quickly inspecting the resulting AKARI/FIS images (Figure 1 and Supplementary Figures ?? through ??), we immediately notice that the central star is in general still the dominant emission source even at these far-IR wavelengths. This is especially true in the SW bands, and quite often so even in the WIDE-L band. Nevertheless, we find many sources with a faint extended CDS.

While we leave detailed analyses into the CDS structures to the next installment of the present series, we briefly comment on the general characteristics of the CDS structures that we can observe from a quick inspection. Many sources appear to be associated with a round extended CDS, some are very obvious (up to about 5' radius) and others are less so. Such sources, of which a few have been previously presented elsewhere, include I04330, I05524 (Ueta et al. 2008), I10329 (Izumiura et al. 2011), I10350, I10580, I12427, I13462, I15465, I15094, I18537, and I23558 (Ueta et al. 2010).

There are many sources whose emission core appears to be more extended than that of the PSF at varying degrees. These objects can also be identified as those whose internal contours are more widely spaced. Such sources include I01037, I02108, I02522, I03062, I03374, I04361, I05251, I06176, I09452, I10223, I10416, I11385, I12380, I13370, I14003, I14219, I16011, I17028, I19390, I19434, AFGL2688, NGC7027, I21419, I22035, I22196, and I23166. Those showing an especially extended emission core are I00248, I11119, I18517, I19574, and I20120. Some of these sources have been found extended in resolved far-IR images taken by Herschel (e.g., I00248, I10329, and I19390; Kerschbaum et al. 2010). Many others seem at least marginally extended, and they need more detailed analyses before concluding anything.

Another group of sources that is worth mentioning here is those that show some indications of interactions between the CDS and ISM. Such cases have been detected in the far-IR around evolved stars and suggested to exist rather commonplace (e.g., Ueta et al. 2006; Ueta et al. 2010; Ueta 2011; Jorissen et al. 2011; Cox et al. 2012; Mayer et al. 2013; Mayer et al. 2014). Such objects are I03463, I04459, I13001, I16255, I18216, I20038, I21412, I22017, I22272, and I23416.

GK Per is an unusual magnetic cataclysmic variable

star that went into a nova in 1901 and the remnant of the outburst is presently seen as a nebula of about 100'' diameter (Slavin et al. 1995). This system, recently undergoing outbursts roughly every 3 years, exhibited a longer-than-normal outburst in 2006 (Evans et al. 2009). This motivated us to observe this system in the far-IR to see if there is any cold thermal dust emission. However, no appreciable far-IR emission was detected in all four AKARI bands.

Overall, we typically find at least a couple of marginally extended sources in each of the 29 panels of images presented. Thus, about 60-70% of the observed objects, roughly speaking, appear to exhibit some kind of extension of the CDS in the far-IR. Many extended objects, especially those listed above, appear to be large enough that its inner shell structure is resolved and can be revealed after the effects of the bright central star is suppressed. Hence, careful central star removal will have to be performed to fully assess the nature of the extended CDSs of evolved stars in the far-IR. Such an analysis will be the main topic of the next installment of the present series of papers (Torres et al. *in preparation*).

7.2 Comparison with the IRAS PSC and AKARI/FIS BSC Entries

One of the main purposes of AKARI is to perform a census of far-IR objects in the whole sky (Yamamura et al. 2009). Hence, there must be corresponding catalog entries for all MLHES sources, as the MLHES targets are essentially selected from the IRAS catalog (i.e., bright enough for AKARI). Thus, as a quick consistency check, we compare the flux densities of the MLHES targets determined by our method with their counterparts in the AKARI/FIS Bright Source Catalog Ver.2 (BSCv2; Yamamura et al. 2016)⁵. We compare only those whose quality flag is 3 (the presence of the source is confirmed and its flux determined to be valid in BSCv2).

Here, we need to remind ourselves that the flux density entries in BSCv2 are measured by yet another independent method, dedicated to produce BSC flux entries with the assumption that the signal is always caused by a point source (Yamamura et al. 2009). Moreover, BSCv2 flux entries are calibrated by a direct comparison with the point-source calibration standard fluxes and not from the surface brightness maps as in our method presented in this work. These differences practically mean that the BSCv2 flux density entries for the MLHES target sources tend to miss contributions from the extended parts of the CDS around the central star. However, the severities of this potential

⁵ Available via <http://www.ir.isas.jaxa.jp/AKARI/Archive/>.

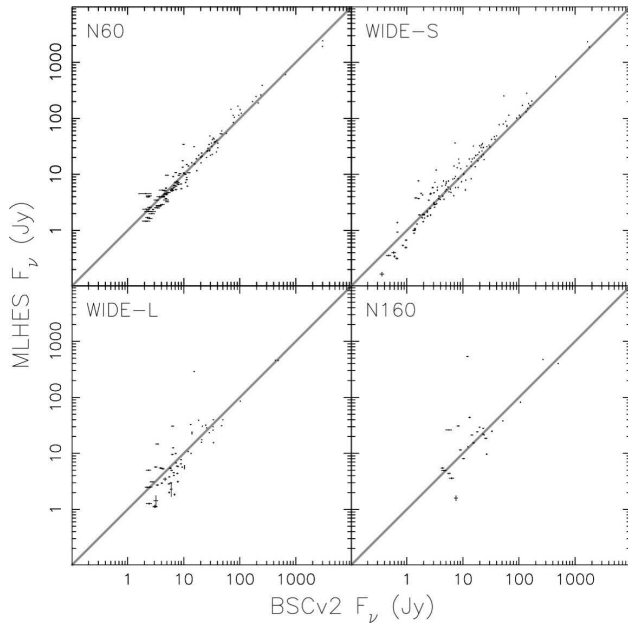


Fig. 2. Comparisons between our photometry measurements and BSCv2 flux density catalog entries in each of the four AKARI bands, N60, WIDE-S, WIDE-L, and N160, from top left to bottom right, in a log-log plot. Uncertainties are shown as error bars. The gray line shows a locus of points at which both flux density values are equal (i.e., the $y = x$ line).

flux density underestimate would depend on the actual appearance of the target sources in the AKARI focal plane. Hence, BSCv2 entries may not always underestimate flux densities of the MLHES sources.

Figure 2 shows the direct comparison between the photometry results of the MLHES targets and their counterparts in BSCv2. In general, our photometry results are consistent with their BSCv2 counterparts, as seen from the distribution of data points that follows the $y = x$ line in gray. However, there is also a relatively large scatter in the distribution of the data points. The width of the scatter is therefore interpreted as the manifestation of this intrinsic difference between the way photometry is done by us and for BSCv2. While there is this subtle difference between our measurements and BSC entries, blind power-law fitting of all the data points yield $F_{\text{N60(MLHES)}} = 1.311 \pm 0.005 F_{\text{N60(BSC)}}^{(0.958 \pm 0.001)}$, $F_{\text{WIDE-S(MLHES)}} = 1.116 \pm 0.003 F_{\text{WIDE-S(BSC)}}^{(1.063 \pm 0.001)}$, $F_{\text{WIDE-L(MLHES)}} = 0.759 \pm 0.004 F_{\text{WIDE-L(BSC)}}^{(1.063 \pm 0.001)}$, and $F_{\text{N160(MLHES)}} = 0.802 \pm 0.009 F_{\text{N160(BSC)}}^{(1.069 \pm 0.002)}$, for N60, WIDE-S, WIDE-L, and N160, respectively. The derived power-law indices are indeed fairly close to unity, and hence, we consider that our photometry results are reasonable.

7.3 Far-IR Colors of the Evolved Star CDS

After the IRAS all-sky survey, van der Veen & Habing (1988) proposed that IRAS two-color diagrams can be used to distinguish C- and O-rich CDSs and put these stars align with the evolutionary sequence. Here, we attempt similar exercise with AKARI two-color diagrams. However, no colors based purely on AKARI flux densities yields any informative distribution of source in any AKARI two-color space, because (1) AKARI's bands are defined over a relatively smaller range of wavelengths and (2) there is a significant overlap between the N60 and WIDE-S bands and the WIDE-L and N160 bands, respectively. Hence, after experimenting with various photometry data in the infrared, we settle with the WISE W2 band (Cutri et al. 2012), because WISE data are among the latest and this band appears least likely to be contaminated by some line emission.

Figure 3 shows the distribution of the MLHES sources in the [65-90] vs. [4.6-65] two-color diagram⁶. Many sources cluster in the region of [65-90] < 0 and [4.6-65] < 0. From this clustering of sources in the [65-90]-[4.9-65] color space, it appears that there are two loci, one horizontal and one vertical, along which other sources are found. In Figure 3, sources located along the tips of these loci are identified. Interestingly, sources at the tip of the horizontal locus (i.e., those with redder [4.6-65] colors) are found to be exclusively PNe, while those at the tip of the vertical locus (i.e., those with redder [65-90] colors) are AGB stars already associated with extended CDSs.

The [65-90] color essentially determines where the dust emission peak is in the spectral energy distribution. That is, if the dust emission peaks at the blueward of $65 \mu\text{m}$ the color is blue (negative), at around $65 - 90 \mu\text{m}$ the color is gray (around zero), and the redward of $90 \mu\text{m}$ the color is red (positive). Meanwhile, the [4.6-65] color compares the relative strength between the stellar emission and the dust emission. While the CDS is being developed during the mass-losing phase the [4.6-65] color is still quite blue, because the flux at $4.6 \mu\text{m}$ from the cold central star is strong. However, when the CDS is fully developed the [4.6-65] color would be reddened, because the flux at $90 \mu\text{m}$ from the CDS is now full-fledged. Hence, this two-color diagram allows us to determine which sources are likely to have an extended CDS and perform central source subtraction in characterizing further the intrinsic CDS structures for the second installment of the series.

⁶ The color is defined to be $[a - b] = -2.5 \log(F_a/F_b)$, where F_a and F_b are flux densities in the band a and b, respectively.

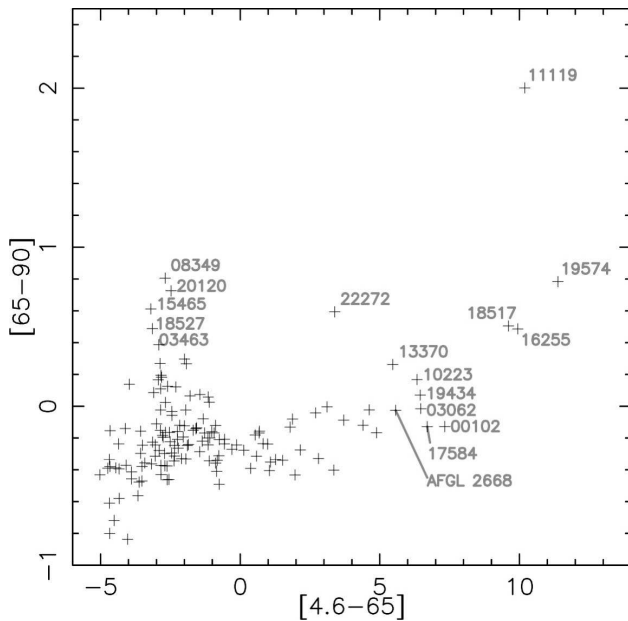


Fig. 3. The distribution of the MLHES targets in the [65-90] vs. [4.6-65] two-color diagram. Sources found along the tips of horizontal and vertical loci emanating from the clustering of sources tend to be associated with an extended CDS and their names are shown.

7.4 Newly Resolved Sources

AKARI’s spatial resolutions are superior with respect to those previously achieved by IRAS and ISO. Indeed, we find 29 instances in 28 targets in which another source is resolved in the immediate vicinity of the MLHES target sources (within the $13'.3 \times 13'.3$ FoV shown; two nearby sources are found in one case). These newly-resolved nearby sources are most likely blended with the target sources themselves when previously observed with IRAS and/or ISO. Most of these newly resolved sources are point sources and fainter than the main target source. However, in a few cases the newly found sources are almost comparable to the main target in brightness. Furthermore, there are several cases in which these nearby sources appear extended (sometimes more than the main target).

Such newly resolved sources are summarized in Table 5, with their coordinates, photometry results, and their nature. We use the Simbad database⁷ to query the AKARI coordinates of these newly resolved sources to see if any of these sources have been recognized previously. When a previously known source is found within the FWHM of the PSF, we associate the AKARI detection to such a source. Out of 29 objects newly resolved by AKARI, 17 are found to have been previously known as identified in Table 5. Of which, 14 are identified to be galaxies, while the rest is simply known as an IR or a radio source. Below, we briefly

comment on each of these newly resolved sources.

Those associated with I00042 (3’ to S), I00245 (2’ to E), I04020 (3’ to SW, extended), I04387 (4’ to NE), I05096 (2’ to S), I07245 (5’ to S, the farther of the two), I10323 (6’ to S), I14567 (4.5’ to W), I18527 (2’ to S, the closer of the two) I21197 (2’ to NE), I21440 (3’ to NE, extended), and I23013 (4.5’ to N) are previously “unknown” (i.e., no corresponding object found after Simbad queries). Given that the majority of the previously known sources are galaxies, these presently unknown sources are most probably galaxies. However, two of these presently unknown sources are extended: we will investigate their nature in future.

8 Summary

Using the FIS on-board the AKARI IR astronomical satellite, we carried out a far-IR imaging survey of the CDSs of 144 evolved stars as one of the AKARI mission programmes that supplemented the satellite’s all-sky survey observations. With this survey we collected far-IR images of roughly $10' \times 40'$ or $10' \times 20'$ around the target evolved stars at 65, 90, 140, and $160 \mu\text{m}$ (Figure 1 and Supplementary Figures ?? through ??).

We detect far-IR emission from all but one object (nova GK Per) at the spatial resolution about $30'' - 50''$. Roughly 60–70% of the detected sources are found extended, to be followed up with more rigorous central source subtraction to isolate the CDS, which will be discussed in the second installment of the present series. With AKARI’s better spatial resolution in comparison with the previous IRAS and ISO images, 29 new sources are now resolved separately around 28 target sources in the very vicinity of the targets. About half of the newly-resolved sources (17/29) turn out to be previously known sources, and the majority (14/17) happens to be galaxies. Hence, the majority of previously unknown sources is also expected to be galaxies. However, there are two extended nearby sources that are previously unidentified, and they will be followed up in future.

The results of photometry measurements (Table 3) are reasonable with respect to the entries in the AKARI/FIS BSCv2, despite the fact that the targets are assumed to be point-sources when the BSCv2 catalogue flux densities were computed. We also tabulate the measured far-IR sky surface brightness in MJy sr^{-1} at the positions of the MLHES targets as a future reference (Table 4). The AKARI-WISE two-color diagram of [65-90] vs. [4.6-65] appears to indicate the progression of the evolution of the CDSs as the CDS becomes more extended and colder (i.e., redder) as time passes. Hence, this two-color diagram can be an ideal tool to determine which sources are likely to

⁷ <http://simbad.u-strasbg.fr/simbad/>

have an extended CDS and perform PSF subtraction in characterizing further the intrinsic CDS structures for the second installment of the series.

Acknowledgments

This research is based on observations with AKARI, a JAXA project with the participation of ESA. TU recognizes partial support from the Japan Society for the Promotion of Science (JSPS) through a FY2013 long-term invitation fellowship program (L13518). RLT was partially supported by the NSF EAPSI Program (OISE-1209948). This research has made use of the SIMBAD database, operated at CDS, Strasbourg, France, as well as data products from the Wide-field IR Survey Explorer, which is a joint project of the University of California, Los Angeles, and the Jet Propulsion Laboratory/California Institute of Technology, funded by NASA. Authors also thank the anonymous referee for his/her valuable comments to improve on the clarity of the manuscript.

Supplementary Data

The following supplementary data is available at PASJ online.

Supplementary Figures 1–28.

Appendix 1 Revised Scaling Parameters for the Power-Law FIS Response Function

A.1.1 Background

The AKARI/FIS slow-scan maps need to be re-calibrated depending on the science to be done with the maps unless the science targets are the diffuse background emission, with which the maps are absolutely calibrated (Doi et al. 2015). For point sources, measured fluxes need to be re-scaled to yield corrected fluxes (Shirahata et al. 2009), whereas for slightly extended objects such as circumstellar shells, surface brightness maps themselves must be re-scaled before fluxes can be correctly measured (Ueta et al. 2017). These re-calibration steps are necessary because the sensitivity of the FIS detector arrays is dependent on the strength of the incoming signal (Matsuura et al. 2011).

The basis of the surface brightness correction method for AKARI/FIS maps is that the PSF shape always remains the same irrespective of the source flux (i.e., scale invariance). This particular characteristic of the FIS detector arrays permit us to describe the FIS response function as a power-law. Therefore, a specific set of parameters for the adopted FIS power-law function (the n and c values; §5) would specifically describe the way the FIS detector arrays responded to incoming signals to yield the specific PSF shape (Ueta et al. 2017).

In characterizing this FIS response function, Ueta et al. (2017) previously used the Gaussian gridding convolution function (GCF) of the beam (FWHM) size of 30'' and 50'' for the SW and LW bands, respectively, upon converting the archived AKARI/FIS TSD into 2-D co-added maps with FAST. These numbers were chosen to keep the consistency between the AKARI FIS All-Sky Survey (AFASS) images and the FIS slow-scan maps. However, this particular parameter choice was not the best if the angular resolution of the resulting co-added images of the FIS slow-scan maps was to be optimized. This is because the kernel size for the point-spread-function (PSF) profile adopted was roughly 1.7 times greater than the intrinsic diffraction limit of AKARI at the wavelength of the wide bands at 90 and 140 μm .

Thus, we need to re-define parameters of the FIS power-law scaling function that are optimized for the present investigation in which the spatial resolution is the utmost importance. In other words, in the present investigation we aim to recover the intrinsic diffraction limit of AKARI at the wavelength of the wide bands at 90 and 140 μm , and hence, we have to use the GCF that represents to the PSF shape at AKARI's intrinsic diffraction limit. Hence, the n and c parameters of the FIS power-law scaling function (s ; §5) must be updated according to the newly adopted PSF shape at the intrinsic diffraction limit.

A.1.2 Super-PSF of the FIS Slow-Scan Maps at AKARI's Diffraction Limit

For the present analysis in which we aim to produce AKARI/FIS images of the highest spatial resolution, we adopt the GCF mimicking the Airy disk of 33'' and 51'' for SW and LW, respectively (i.e., the intrinsic diffraction limit of AKARI at these wavelengths). The effective Airy disk size (defined to be of the $1/e^2$ diameter) measured from the resulting super-PSFs turns out to be 49''.1 and 76''.7, while the effective FWHM is 23''.3 and 34''.9. Thus, the effective FWHM size is roughly a factor of 2 smaller in the present study with respect to those used by Ueta et al. (2017).

Fig. 4 shows the “super-PSF” images of the intrinsic diffraction limit in the four AKARI/FIS bands, made by taking the median of the normalized FAST-processed FIS maps of the PSF/photometric reference sources (using 24 and 18 sources for the SW and LW bands, respectively; Table 1 of Ueta et al. 2017). The median MADs intrinsic to the source emission are found to be $0.2 \pm 0.1\%$, $0.3 \pm 0.2\%$, $2.1 \pm 1.1\%$, and $4.1 \pm 2.1\%$, for the N60, WIDE-S, WIDE-L, and N160 bands, respectively, within the $5\text{-}\sigma$ region (dashed contour in the PSF images), almost identi-

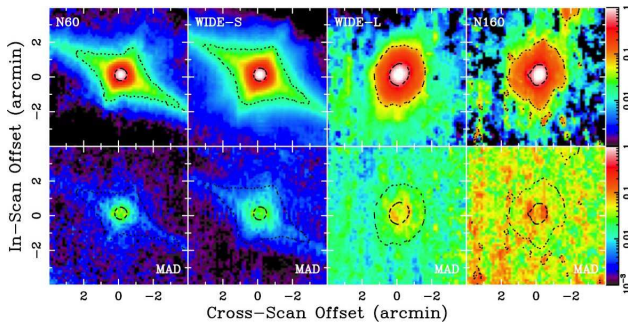


Fig. 4. The AKARI/FIS super-PSF images (top row) and the corresponding median absolute deviation (MAD) maps (bottom row) in the N60, WIDE-S, WIDE-L, and N160 bands (top row; from left to right). The logarithmic color scaling of the images, from 0.1% to 100% relative to the peak intensity, is indicated in the wedge on the right. The dashed and dotted contours in the PSF surface brightness distribution images represent the FWHM and 5σ levels, respectively.

cal to the previous cases (Ueta et al. 2017).

A.1.3 Determination of the Updated Scaling Factors

We follow exactly the same procedure as described by Ueta et al. (2017) in deriving the power-law FIS response function n and c scaling factors. In a nutshell, we fine-tune the n and c parameters until the resulting “corrected” measured fluxes reproduce the “expected” values of far-IR photometric calibration objects (Shirahata et al. 2009; Ueta et al. 2017). The derived parameters are shown in Table 2. Here, we just present the comparison ratio between the corrected and expected PSF fluxes as a function of the expected PSF flux for each FIS band in Fig. 5. The power-law fits of the corrected-to-expected PSF flux ratios are $(1.01 \pm 0.03) \times F_{\text{Jy}}^{(-0.009 \pm 0.007)}$, $(0.99 \pm 0.02) \times F_{\text{Jy}}^{(0.019 \pm 0.006)}$, $(1.04 \pm 0.03) \times F_{\text{Jy}}^{(-0.036 \pm 0.008)}$, and $(1.04 \pm 0.03) \times F_{\text{Jy}}^{(-0.027 \pm 0.010)}$, respectively, for the N60, WIDE-S, WIDE-L, and N160 bands, where F_{Jy} is the 3σ expected flux in Jy. Compared with the previous case, the present re-scaling is a few percent better in the SW band and equally good in the LW band. This suggests that the quality of the results of the flux calibration does not differ much by the choice of the PSF shape (i.e., the GCF parameters).

References

Acker, A., Marcout, J., Ochsenbein, F., et al. 1992, The Strasbourg-ESO Catalogue of Galactic Planetary Nebulae. Parts I, II. (Garching: European Southern Observatory)

Arimatsu, K., Izumiura, H., Ueta, T., et al. 2011, ApJL, 729, L19

Beichman, C. A., Neugebauer, G., Habing, H. J., et al.

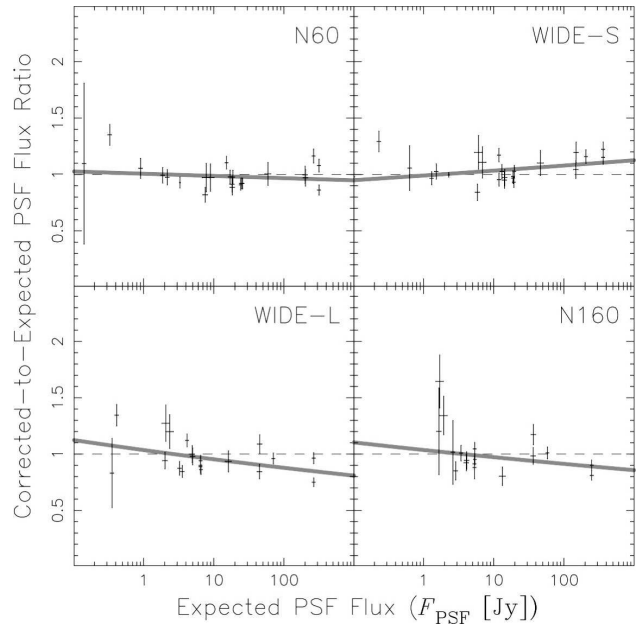


Fig. 5. The corrected-to-expected PSF flux ratios as a function of the expected PSF flux in each of the AKARI/FIS bands. The expected fluxes are the previously known fluxes of the far-IR flux calibration objects used in the analysis, while the corrected fluxes are those measured from the AKARI/FIS maps rescaled with the parameters in Table 2. The gray solid lines show the power-law best fits. These plots, compared with Fig. 5 of Ueta et al. (2017), confirm that the revised surface brightness correction applied to the raw/archived FIS maps suppressed the signal-strength-dependent response of the FIS detector in the FAST-processed FIS maps better.

1989, IRAS Point Source Reject Catalog, Version 2.1 (Washington, D.C.: NASA GPO)

Chan, S. J., & Kwok, S. 1988, ApJ, 334, 362

Cox, N. L. J., García-Hernández, D. A., García-Lario, P., et al. 2011, AJ, 141, 111

Cox, N. L. J., Kerschbaum, F., van Marle, A.-J., et al. 2012, A&A, 537, A35

Cutri, R. M., Wright, E. L., Conrow, T., et al. 2012, Explanatory Supplement to the WISE All-Sky Data Release Products (Pasadena: IPAC/Caltech)

Decin, L., Cox, N. L. J., Royer, P., et al. 2012, A&A, 548, A113

Do, T., Morris, M., Sahai, R., & Stapelfeldt, K. 2007, AJ, 134, 1419

Doi, Y., Hirooka, S., Sato, A., et al. 2002, Advances in Space Research, 30, 2099

Doi, Y., Takita, S., Ootsubo, T., et al. 2015, PASJ, 67, 50

Evans, P. A., Beardmore, A. P., Osborne, J. P., & Wynn, G. A. 2009, MNRAS, 399, 1167

Fujiwara, M., Hirao, T., Kawada, M., et al. 2003, Appl. Opt., 42, 2166

Gillett, F. C., Backman, D. E., Beichman, C., & Neugebauer, G. 1986, ApJ, 310, 842

Groenewegen, M. A. T., Waelkens, C., Barlow, M. J., et al. 2011, A&A, 526, A162

Habing, H. J., Olmon, F. M., Chester, T., Gillett, F., & Rowan-Robinson, M. 1985, A&A, 152, L1

Hacking, P., Neugebauer, G., Emerson, J., et al. 1985, PASP,

- 97, 616
- Hashimoto, O., & Izumiura, H. 1998, *Ap&SS*, 255, 349
- Hashimoto, O., Izumiura, H., Kester, D. J. M., & Bontekoe, T. R. 1998, *A&A*, 329, 213
- Herwig, F. 2005, *ARA&A*, 43, 435
- Höfner, S., & Olofsson, H. 2018, *A&ARv*, 26, 1
- Iben, I. 2012, *Stellar Evolution Physics* (Cambridge: CUP)
- Ikeda, N. 2012, *FAST User's Handbook*, ver. 0.1 (Sagamihara: ISAS)
- Izumiura, H., Hashimoto, O., Kawara, K., Yamamura, I., & Waters, L. B. F. M. 1996, *A&A*, 315, L221
- Izumiura, H., Ueta, T., Yamamura, I., et al. 2009, *ASP Conf. Ser.* 418: *AKARI, a Light to Illuminate the Misty Universe*, eds. T. Onaka, G. J. White, T. Nakagawa, & I. Yamamura (San Francisco: ASP), 127
- Izumiura, H., Ueta, T., Yamamura, I., et al. 2011, *A&A*, 528, A29
- Izumiura, H., Waters, L. B. F. M., de Jong, T., et al. 1997, *A&A*, 323, 449
- Jackson, T., Ivezić, Ž., & Knapp, G. R. 2002, *MNRAS*, 337, 749
- Jorissen, A., Mayer, A., van Eck, S., et al. 2011, *A&A*, 532, A135
- Kaneda, H., Okamura, Y., Nakagawa, T., & Shibai, H. 2002, *Advances in Space Research*, 30, 2105
- Karakas, A. I., & Lattanzio, J. C. 2014, *PASA*, 31, e030
- Kawada, M., Baba, H., Barthel, P. D., et al. 2007, *PASJ*, 59, S389
- Kerschbaum, F., Ladjal, D., Ottensamer, R., et al. 2010, *A&A*, 518, L140
- Kessler, M. F., Steinz, J. A., Anderegg, M. E., et al. 1996, *A&A*, 315, L27
- Kimeswenger, S., & Kienel, C. 1997, *ASSL Vol. 210: The Impact of Large Scale Near-IR Sky Surveys*, eds. F. Garzón, N. Epchtein, A. Omont, B. Burton, & P. Persi (Dordrecht: Kluwer), 105
- Knauer, T. G., Ivezić, Ž., & Knapp, G. R. 2001, *ApJ*, 552, 787
- Maercker, M., Mohamed, S., Vlemmings, W. H. T., et al. 2012, *Nature*, 490, 232
- Marton, G., Calzoletti, L., Perez Garcia, A. M., et al. 2017, *The Herschel/PACS Point Source Catalogue Explanatory Supplement Ver. 2.2* ()
- Matsuura, S., Shirahata, M., Kawada, M., et al. 2007, *PASJ*, 59, S503
- Matsuura, S., Shirahata, M., Kawada, M., et al. 2011, *ApJ*, 737, 2
- Mayer, A., Jorissen, A., Kerschbaum, F., et al. 2013, *A&A*, 549, A69
- Mayer, A., Jorissen, A., Paladini, C., et al. 2014, *A&A*, 570, A113
- Meixner, M., Campbell, M. T., Welch, W. J., & Likkell, L., 1998, *ApJ*, 509, 392
- Meixner, M., Ueta, T., Bobrowsky, M., & Speck, A. 2002, *ApJ*, 571, 936
- Meixner, M., Ueta, T., Dayal, A., et al. 1999, *ApJS*, 122, 221
- Moshir, M., Copan, G., Conrow, T., et al. 1990, *IRAS Faint Source Catalogue*, version 2.0 (Washington, D.C.: NASA GPO)
- Murakami, H., Baba, H., Barthel, P., et al. 2007, *PASJ*, 59, S369
- Neugebauer, G., Habing, H. J., van Duinen, R., et al. 1984, *ApJL*, 278, L1
- Noriega-Crespo, A., van Buren, D., Cao, Y., & Dgani, R. 1997, *AJ*, 114, 837
- Otsuka, M., Ueta, T., van Hoof, P. A. M., et al. 2017, *ApJS*, 231, 22
- Paczyński, B. 1971, *Acta Astronom*, 21, 417
- Pilbratt, G. L., Riedinger, J. R., Passvogel, T., et al. 2010, *A&A*, 518, L1
- Renzini, A. 1981, *Astrophysics and Space Science Library 88: Physical Processes in Red Giants*, eds. I. Iben, Jr. & A. Renzini (Dordrecht: D. Reidel), 431
- Sahai, R., Morris, M., Sánchez Contreras, C., & Claussen, M. 2007, *AJ*, 134, 2200
- Shirahata, M., Matsuura, S., Hasegawa, S., et al. 2009, *PASJ*, 61, 737
- Siódmiak, N., Meixner, M., Ueta, T., et al. 2008, *ApJ*, 677, 382-400
- Slavin, A. J., O'Brien, T. J., & Dunlop, J. S. 1995, *MNRAS*, 276, 353
- Speck, A. K., Meixner, M., & Knapp, G. R. 2000, *ApJL*, 545, L145
- Stencel, R. E., Pesce, J. E., & Hagen Bauer, W. 1988, *AJ*, 95, 141
- Suzuki, T., Kaneda, H., Matsuura, S., et al. 2008, *PASP*, 120, 895
- Szczerba, R., Siódmiak, N., Stasińska, G., & Borkowski, J. 2007, *A&A*, 469, 799
- Takita, S., Doi, Y., Ootsubo, T., et al. 2015, *PASJ*, 67, 51
- Ueta, T. 2011, *ASP Conf. Ser.* 445 *Why Galaxies Care about AGB Stars II: Shining Examples and Common Inhabitants* (San Francisco: ASP), 295
- Ueta, T., Meixner, M., & Bobrowsky, M. 2000, *ApJ*, 528, 861
- Ueta, T., Izumiura, H., Yamamura, I., et al. 2007, *AIP Conf. Proceedings 948: Unsolved Problems in Stellar Physics: A Conference in Honor of Douglas Gough*, eds. R. J. Stancliffe, G. Houdek, R. G. Martin, & C. A. Tout (Cambridge: AIP), 365
- Ueta, T., Izumiura, H., Yamamura, I., et al. 2008, *PASJ*, 60, S407
- Ueta, T., Ladjal, D., Exter, K. M., et al. 2014, *A&A*, 565, A36
- Ueta, T., Speck, A. K., Stencel, R. E., et al. 2006, *ApJL*, 648, L39
- Ueta, T., Stencel, R. E., Yamamura, I., et al. 2010, *A&A*, 514, A16
- Ueta, T., Tomasino, R. L., Takita, S., et al. 2017, *PASJ*, 69, 11
- van der Veen, W. E. C. J., & Habing, H. J. 1988, *A&A*, 194, 125
- Verdugo, E., Yamamura, I., & Pearson, C. 2007, *AKARI FIS Data User Manual*, ver. 1.3 (Sagamihara: ISAS)
- Waters, L. B. F. M., Loup, C., Kester, D. J. M., Bontekoe, T. R., & de Jong, T. 1994, *A&A*, 281, L1
- Weidemann, V. 1990, *ARA&A*, 28, 103
- Werner, M. W., Roellig, T. L., Low, F. J., et al. 2004, *ApJS*, 154, 1

- Willems, F. J., & de Jong, T. 1988, *A&A*, 196, 173
- Yamamura, I., et al. 2009, in *Astronomical Society of the Pacific Conference Series Vol. 418, AKARI, a Light to Illuminate the Misty Universe*, eds. Onaka, T., White, G. J., Nakagawa, T., & Yamamura, I., p. 3
- Yamamura, I., Makiuti, S., & the AKARI team 2016, *AKARI-FIR Bright Source Catalogue Public Version 2 Release Note*
- Young, K., Phillips, T. G., & Knapp, G. R. 1993a, *ApJS*, 86, 517
- Young, K., Phillips, T. G., & Knapp, G. R. 1993b, *ApJ*, 409, 725

Table 1. Target List and Observation Log

Target Name ^a	Alt. Name	RA(J2000)	DEC(J2000)	Type ^b	Var. ^c	Sp. Type	Obs. Date	Obs. Time	Publ. Ref.	OBSID	AOTPARAM ^d
IRAS 00042+4248	KU And	00:06:52.752	+43:05:02.25	Mi*	M	M10	7/14/07	19:41:56	1995	1711042-001	1.0;15;70
IRAS 00102+7214	NGC 40	00:13:01.01014	+72:31:19.0944	PN	...	[WC8]	8/15/07	17:39:06	1995	1711293-001	1.0;15;70
IRAS 00128-3219	S Scl	00:15:22.26580	-32:02:42.9899	Mi*	M	M7/8IIIe	6/10/07	18:50:30	1995	1711091-001	1.0;15;70
IRAS 00245-0652	UY Cet	00:27:06.4494	-06:36:16.871	AB*	SRB	M7	6/25/07	21:42:31	1995	1711023-001	1.0;15;70
IRAS 00248+3518	AQ And	00:27:31.68373	+35:35:14.5034	C*	SR	C	7/14/07	21:23:34	1995	1711226-001	1.0;15;70
IRAS 00254-3317	η Scl	00:27:55.69870	-33:00:25.7977	LP*	LB	M2/3III	6/12/07	13:56:01	1995	1711122-001	2.0;8;70
IRAS 01037+1219	IRC +10011	01:06:25.984	+12:35:53.05	OH*	M	M8	7/12/07	14:47:31	1995	1711040-001	0.5;15;70
IRAS 01144+6658	RAFGL 190	01:17:51.378	+67:13:53.34	C*	M	...	8/15/07	21:00:33	1995	1711305-001	1.0;15;70
IRAS 01246-3248	R Scl	01:26:58.09492	-32:32:35.4374	C*	SRB	C6,4	6/27/07	21:54:39	1995	1711031-001	1.0;15;70
IRAS 01556+4511	V370 And	01:58:44.32868	+45:26:06.8989	AB*	LB:	M8	2/3/07	15:12:25	1995	17110035-001	1.0;15;70
IRAS 02143+4404	W And	02:17:32.96107	+44:18:17.7691	S*	M	S7-8/1e-M7Se	8/11/07	1:02:03	1995	1711106-001	1.0;15;70
IRAS 02168-0312	σ Cet	02:19:20.79210	-02:58:39.4956	Mi*	M	M5-9IIIe+DA	1/21/07	14:09:34	1995	1710026-001	0.5;15;70
IRAS 02302+4525	UX And	02:30:28.803	+45:39:15.78	LP*	SRB	M6IIIv	8/14/07	18:35:59	1995	1711078-001	1.0;15;70
IRAS 02427-5430	W Hor	02:44:14.7520	-54:18:04.108	LP*	SRB	M5/7	12/25/06	8:16:44	1995	1710055-001	1.0;15;70
IRAS 02464-5915	X Hor	02:47:44.947	-59:03:04.22	Mi*	SRA	M6/8	6/16/07	15:52:20	1995	1711168-001	2.0;8;70
IRAS 02522-5005	R Hor	02:53:52.77206	-49:53:22.7408	Mi*	M	M5-7e	1/2/07	4:55:22	1995	1711030-001	1.0;15;70
IRAS 03019+3838	ρ Per	03:05:10.59385	+38:50:24.9943	LP*	SRB	M4+IIIa	8/18/07	13:50:37	1995	1711602-001	1.0;15;70
IRAS 03062+6107	IC 289	03:10:19.30	+61:19:01.0	PN	2/23/07	13:40:38	1995	1710142-001	1.0;15;70
IRAS 03112-5730	TW Hor	03:12:33.15984	-57:19:17.5790	C*	SRB	C7,2	6/28/07	21:15:38	1995	1711084-001	1.0;15;70
IRAS 03172-2156	τ ⁰⁴ Eri	03:19:31.00224	-21:45:28.3049	LP*	LB	M3III-IIIaCa-1	8/2/07	20:00:29	1995	1711002-001	2.0;8;70
GK Per	Nova Per 1901	03:31:12.012	+43:54:15.48	No*	...	Be+K2sdI*	8/24/07	17:26:35	1995	1711603-001	1.0;15;240
IRAS 03374+6229	U Cam	03:41:48.17393	+62:38:54.3906	C*	SRB	C5,4_MS4	2/27/07	23:37:33	1995	1710123-001	1.0;15;70
IRAS 03463-0710	BR Eri	03:48:47.52714	-07:00:53.9463	LP*	SRB	M5V	8/15/07	23:02:33	1995	1711012-001	1.0;15;70
IRAS 04020-1551	V Eri	04:04:18.79987	-15:43:30.5145	AB*	SRC	M7+II:	8/18/07	2:29:33	1995	1711010-001	1.0;15;70
IRAS 04330-6307	R Ret	04:33:32.83035	-63:01:45.0103	Mi*	M	M6.5e	6/30/07	23:02:31	1995	1711173-001	2.0;8;70
IRAS 04361-6210	P Dor	04:36:45.59127	-62:04:37.7974	AB*	SRB	M8III:e	1/4/07	4:49:33	1995	1710014-001	0.5;15;70
IRAS 04387-3819	R Cae	04:40:30.08596	-38:14:06.9557	Mi*	M	M6e	2/16/07	10:41:18	1995	1710063-001	1.0;15;70
IRAS 04459+6804	ST Cam	04:51:13.34776	+68:10:07.6182	C*	SRB	C5,4_MS2	3/11/07	18:46:35	1995	1710307-001	1.0;15;70
IRAS 04573-1452	R Lep	04:59:36.34904	-14:48:22.5309	C*	M	C7,6e	3/2/07	7:33:40	1995	1710031-001	1.0;15;70
IRAS 05071-6327	WZ Dor	05:07:34.02861	-63:23:58.8365	LP*	SRB	M3III	7/14/07	23:34:21	1995	1711136-001	2.0;8;70
IRAS 05096-4834	S Pic	05:10:57.24760	-48:30:25.4481	Mi*	M	M7e	2/22/07	9:00:37	1995	1710064-001	1.0;15;70
IRAS 05251-1244	IC 418	05:27:28.2037	-12:41:50.265	PN	NL:	O7fp	3/10/07	9:17:22	1995	1710310-001	0.5;15;70
IRAS 05411-8625	R Oct	05:26:06.19562	-86:23:17.7741	Mi*	M	M5.5e	3/22/07	23:58:43	1995	1710315-001	1.0;15;70
IRAS 05418-4628	W Pic	05:43:13.8307	-46:27:13.828	C*	LB	C-J5_C2_6_j7_MS3	9/13/06	19:22:48	1995	1710005-001	2.0;15;70
IRAS 05524+0723	α Ori	05:55:10.30536	+07:24:25.4304	s*r	SRC	M1-M2Ia-Iab	9/21/06	22:09:50	1995	1710038-001	0.5;15;70
IRAS 05528+2010	U Ori	05:55:49.16994	+20:10:30.6872	Mi*	M	M6-9.5e	3/19/07	10:21:32	1995	1710317-001	1.0;15;70
IRAS 06176-1036	HD 44179	06:19:58.21855	-10:38:14.7061	pA*	OH/IR/R:	B9Ib/II	9/28/06	21:11:37	1995	1710044-001	0.5;15;70
IRAS 07059-5818	AC Car	07:06:47.96915	-58:22:51.4909	LP*	SRB	M6+III:	5/13/07	13:26:40	1995	1711159-001	1.0;15;70
IRAS 07245+4605	Y Lyn	07:28:11.61802	+45:59:26.2366	S*	SRC	M6S	4/6/07	10:43:09	1995	1710314-001	1.0;15;70
IRAS 08349-5945	KK Car	08:36:01.288	-59:56:26.77	Mi*	M	M3pev	12/18/06	18:53:23	1995	1710025-001	1.0;15;70
IRAS 09200-5805	NGC 2867	09:21:25.38	-58:18:40.9	PN	...	[WO2]	6/25/07	0:38:34	1995	1711304-001	1.0;15;70
IRAS 09429-2148	IW Hya	09:45:15.24	-22:01:45.3	OH*	OH/IR/M:	M8/9	5/28/07	9:53:22	1995	1711045-001	1.0;15;70
IRAS 09452+1330	IRC +10216	09:47:57.406	+13:16:43.56	C*	M	C9,5e	5/15/07	15:30:42	1995	1711241-001	0.5;15;70
Y Hya	CGCS 2641	09:51:03.7179	-23:01:02.351	C*	SRB	C5,4	12/1/06	23:03:05	1995	1710196-001	1.0;15;70
IRAS 10223-1823	NGC 3242	10:24:46.107	-18:38:32.64	PN	12/7/06	19:37:50	1995	1710069-001	1.0;15;70
IRAS 10323-4611	CGCS 6386	10:34:30.98	-46:27:29.1	C*	OH/IR/B	...	12/26/06	18:43:15	1995	1710042-001	1.0;15;70
IRAS 10329-3918	U Ant	10:35:12.85153	-39:33:45.3180	C*	LB	C5,3	12/21/06	16:15:12	1995	1710002-001	1.0;15;70
IRAS 10350-1307	U Hya	10:37:33.27295	-13:23:04.3529	C*	SRB	C6,3_MS2	6/7/07	10:13:48	1995	1711504-001	1.0;15;70
IRAS 10416+6740	VY UMa	10:45:04.03151	+67:24:40.9887	C*	LB	C6,3	10/31/06	7:30:20	1995	1710003-001	1.0;15;70
IRAS 10580-1803	R CrI	11:00:33.85289	-18:19:29.5802	AB*	SRB	M7/8III	6/15/07	10:27:44	1995	1711080-001	1.0;15;70
IRAS 11119+5517	NGC 3587	11:14:47.701	+55:01:08.72	PN	5/13/07	7:23:14	1995	1711114-001	1.0;15;70
IRAS 11125+7524	CS Dra	11:15:55.9033	+75:08:34.564	LP*	LB	M5	10/24/06	8:27:49	1995	1710045-001	1.0;15;70
IRAS 11251+4527	ST UMa	11:27:50.37920	+45:11:06.7628	LP*	SRB	M4III	5/22/07	16:41:13	1995	1711144-001	1.0;15;70
IRAS 11385-5517	HD 101584	11:40:58.8052	-55:34:25.814	pA*	...	B8/9I/IIe	7/19/07	9:53:16	1995	1711275-001	0.5;15;70

Table 1. (Continued)

Target Name ^a	Alt. Name	RA(J2000)	DEC(J2000)	Type ^b	Var. ^c	Sp. Type	Obs. Date	Obs. Time	OBSID	AOTPARAM ^d
IRAS 11461-3542	V919 Cen	11:48:39.22340	-35:59:12.9055	AB*	SRB:	M7III	7/6/07	2:00:27	1711366-001	1.0;15;70
IRAS 11538+5808	Z UMa	11:56:30.22478	+57:52:17.6495	LP*	SRB	M5IIIv	5/17/07	10:49:21	1711073-001	1.0;15;70
IRAS 12380+5607	Y UMa	12:40:21.27880	+55:50:47.6091	AB*	SRB	M7II-III:	11/28/06	10:17:27	1710013-001	1.0;15;70
IRAS 12427+4542	Y CVn	12:45:07.82766	+45:26:24.9249	C*	SRB	C5,4J	12/9/06	11:00:21	1710015-001	1.0;15;70
IRAS 12526+4728	TU CVn	12:54:56.52122	+47:11:48.2021	LP*	SRB	M5-III-IIIa	6/9/07	10:36:06	1711147-001	2.0;8;70
IRAS 12544+6615	RY Dra	12:56:25.91249	+65:59:39.8086	C*	SRB:	C4,5J,MS5	11/17/06	9:36:18	1710017-001	1.0;15;70
IRAS 13001+0527	RT Vir	13:02:37.98140	+05:11:08.3825	AB*	SRB	M8III	7/4/07	15:24:06	1711025-001	1.0;15;70
IRAS 13172+4547	V CVn	13:19:27.76567	+45:31:37.6651	Mi*	SRA	M4-M6e	6/15/07	15:45:43	1711165-001	2.0;8;70
IRAS F13370-3123	Z Cen	13:39:55.90	-31:38:31	SNI	7/5/07	16:51:14	1711285-001	1.0;15;70
IRAS 13462-2807	W Hya	13:49:01.99810	-28:22:03.4881	Mi*	SRA	M7.5-9e	7/28/07	16:13:25	1711236-001	0.5;15;70
IRAS 13468+3947	R CVn	13:48:57.04306	+39:32:33.1687	Mi*	M	M6.5-9e	6/27/07	14:39:21	1711178-001	2.0;8;70
IRAS 14003-7633	θ Aps	14:05:19.87784	-76:47:48.3204	LP*	SRB	M6.5III:	2/28/07	18:44:45	1710010-001	1.0;15;70
IRAS 14162+6701	U UMi	14:17:19.90173	+66:47:39.2153	Mi*	M	M6-8e	5/23/07	19:20:26	1711188-001	1.0;15;70
IRAS 14219+2555	RX Boo	14:24:11.62662	+25:42:13.4091	AB*	SRB	M7.5-M8	1/14/07	12:25:29	1710009-001	1.0;15;70
IRAS 14277+3904	V Boo	14:29:45.26599	+38:51:40.6600	LP*	SRA	M5+-6.5e	7/9/07	3:19:56	1711167-001	2.0;8;70
IRAS 14567+6607	RR UMi	14:57:35.00729	+65:55:56.8569	LP*	SRB	M4.5III	5/30/07	12:05:08	1711070-001	1.0;15;70
IRAS 14591-4438	CGCS 6570	15:02:32.189	-44:50:07.96	OH*	OH/IR/B	...	2/15/07	19:21:24	1710043-001	1.0;15;70
IRAS 15094-6953	X TrA	15:14:19.17535	-70:04:46.1052	C*	LB	C5,5	2/28/07	20:21:49	1710004-001	1.0;15;70
IRAS 15255+1944	WX Ser	15:27:47.043	+19:33:51.71	Mi*	M	M8.5	8/6/07	11:03:34	1711041-001	1.0;15;70
IRAS 15396+3842	RR CrB	15:41:26.22899	+38:33:26.5958	LP*	SRB	M3	7/30/07	11:39:59	1711151-001	2.0;8;70
IRAS 15465+2818	R CrB	15:48:34.4147	+28:09:24.295	RC*	RCB	G0Iep	2/4/07	14:50:59	1710033-001	1.0;15;70
IRAS 15477+3943	V CrB	15:49:31.3120	+39:34:17.890	C*	M	C6,2e,MS3	8/1/07	0:09:12	1711107-001	2.0;8;70
IRAS 15492+4837	ST Her	15:50:46.62569	+48:28:58.8508	S*	SRB	M6S-M7SIII:	1/20/07	20:33:24	1710008-001	1.0;15;70
IRAS 16011+4722	X Her	16:02:39.17325	+47:14:25.2806	AB*	SRB	M6III	1/26/07	15:35:09	1710007-001	1.0;15;70
IRAS 16164+5952	AT Dra	16:17:15.34668	+59:45:18.0832	LP*	LB	M4III	7/7/07	21:37:00	1711003-001	2.0;8;70
IRAS 16255+2801	Abell 39	16:27:33.71	+27:54:33.5	PN	PN	DAO.70	8/20/07	15:05:25	1711221-001	2.0;8;70
IRAS 16306+7223	R UMi	16:29:57.89762	+72:16:49.1681	LP*	SRB	M7III:e	11/4/06	7:17:31	1710053-001	1.0;15;70
IRAS 16418+5459	S Dra	16:42:55.87831	+54:54:13.6149	AB*	SRB	M6III	1/30/07	22:09:59	1710011-001	1.0;15;70
IRAS 16457+4219	V636 Her	16:47:19.74712	+42:14:20.0990	LP*	LB	M4.5III	8/20/07	11:50:50	1711126-001	2.0;8;70
IRAS 16473+5753	AH Dra	16:48:16.63223	+57:48:49.3534	LP*	SRB	M5	7/28/07	11:40:55	1711161-001	2.0;8;70
IRAS 17028-1004	M 2-9	17:05:37.952	-10:08:34.58	PN	...	Be	9/9/06	10:10:51	1710070-001	0.5;15;70
IRAS 17081+6422	TV Dra	17:08:24.50463	+64:19:08.7446	AB*	LB	MS	7/1/07	23:05:38	1711063-001	1.0;15;70
IRAS 17119+0859	IRC +10322	17:14:19.393	+08:56:02.60	AB*	OH/IR/SR:	M9-10	3/7/07	19:12:38	1710041-001	1.0;15;70
IRAS 17389-5742	V Pav	17:43:18.94034	-57:43:26.2886	C*	SRB	C6,4	3/18/07	20:27:35	1710312-001	1.0;15;70
IRAS 17584+6638A	NGC 6543	17:58:33.423	+66:37:59.52	PN	...	[WC]	10/2/06	5:37:22	1710066-001	0.5;15;70
IRAS 18216+6419	DS Dra	18:21:57.2365	+64:20:36.226	PN	...	PG1159	5/8/07	16:36:45	1711215-001	1.0;15;70
IRAS 18517+3257	NGC 6720	18:53:35.079	+33:01:45.03	PN	...	DA(O?)	4/9/07	20:20:33	1710319-001	1.0;15;70
IRAS 18527+3650	δ^{02} Lyr	18:54:30.28335	+36:53:55.0133	LP*	SRC:	M4II	4/12/07	17:53:06	1710318-001	1.0;15;70
IRAS 18537+4352	13 Lyr	18:55:20.10223	+43:56:45.9315	LP*	SRB	M5III	4/14/07	17:53:33	1710344-001	1.0;15;70
IRAS 19143-5032	V Tel	19:18:14.609	-50:26:48.37	LP*	SRB	M6/8	10/7/06	7:24:44	1710051-001	1.0;15;70
IRAS 19233+7627	UX Dra	19:21:35.51795	+76:33:34.5443	C*	SRA:	C7,3	2/22/07	16:19:58	1710016-001	1.0;15;70
IRAS 19314-1629	AQ Sgr	19:34:18.99465	-16:22:27.0363	C*	SRB	C7,4	10/16/06	6:29:15	1710018-001	1.0;15;70
IRAS 19354+5005	R Cyg	19:36:49.381	+50:11:59.46	S*	M	S4-8/6e	11/10/06	10:20:57	1710030-001	1.0;15;70
IRAS 19390+3229	TT Cyg	19:40:57.0158	+32:37:05.757	C*	SRB	C4,4	4/26/07	19:49:51	1710322-001	1.0;15;70
IRAS 19409+5520	V Cyg	19:42:04.1472	+55:27:47.599	LP*	LB	M5III	5/20/07	10:19:58	1711128-001	1.0;15;70
IRAS 19434+5024	NGC 6826	19:44:48.1501	+50:31:30.264	PN	E/SD:	O6fp	11/13/06	17:43:17	1710143-001	0.5;15;70
IRAS 19510-5919	S Pav	19:55:13.96727	-59:11:44.3384	Mi*	SRA	M8III	10/11/06	7:15:50	1710059-001	1.0;15;70
IRAS 19574+2234	NGC 6853	19:59:36.379	+22:43:15.75	PN	...	DAO.6	4/28/07	18:15:52	1710327-001	1.0;15;240
IRAS 19575-5930	NU Pav	20:01:44.74540	-59:22:33.2177	LP*	SRB	M6III	10/12/06	6:23:52	1710049-001	1.0;15;70
IRAS 20038-2722	V Sgr	20:06:55.24418	-27:13:29.7616	AB*	LB	M7/8III	10/21/06	10:26:19	1710046-001	1.0;15;70
IRAS 20075-6005	X Pav	20:11:45.86402	-59:56:12.8172	AB*	SRB	M8III	10/13/06	7:11:33	1710056-001	1.0;15;70
IRAS 20088+4618	NGC 6884	20:10:23.66	+46:27:39.8	PN	5/17/07	2:50:58	1711329-001	1.0;15;70
IRAS 20120-4433	RZ Sgr	20:15:28.4049	-44:24:37.480	S*	SRB	S4,4ep	10/19/06	8:45:14	1710057-001	1.0;15;70
IRAS 20141-2128	RT Cap	20:17:06.52984	-21:19:04.4818	C*	SRB	C6,4	4/21/07	19:09:58	1710320-001	1.0;15;70

Table 1. (Continued)

Target Name ^a	Alt. Name	RA(J2000)	DEC(J2000)	Type ^b	Var. ^c	Sp. Type	Obs. Date	Obs. Time	Filter	OBSID	AOTPARAM ^d
IRAS 20248–2825	T Mic	20:27:55.18840	–28:15:39.8035	AB*	SRB	M7/8III	4/22/07	20:01:59	F450LP	1710316-001	1.0;15;70
IRAS 20396+4757	V Cyg	20:41:18.2687	+48:08:28.822	C*	M	C7,4e	11/29/06	14:06:33	F450LP	1710102-001	0.5;15;70
IRAS R21003+3629	Egg Nebula	21:02:18.27	+36:41:37.0	pA*	SNI	F5Iae	7/28/07	14:32:33	F450LP	1711232-001	1.0;15;70
NGC 7027	NGC 7027	21:07:01.8	+42:14:10:	PN	12/1/06	10:44:54	F450LP	1710207-001	0.5;15;70
IRAS 21197–6956	Y Pav	21:24:16.75016	–69:44:01.9759	C*	SRB	C7,3	10/18/06	6:10:54	F450LP	1710019-001	1.0;15;70
IRAS 21282+5050	PNG 093.9-00.1	21:29:58.470	+51:04:00.30	PN	...	O7(f)/[WC11]	6/16/07	10:19:33	F450LP	1711328-001	1.0;15;70
IRAS 21358+7823	S Cep	21:35:12.82976	+78:37:28.1892	C*	M	C7,3e	2/17/07	13:46:33	F450LP	1710032-001	1.0;15;70
IRAS 21412+3747	RCyg	21:43:16.32871	+38:01:02.9725	C*	SRB	C6,4_MS5	12/7/06	8:58:33	F450LP	1710020-001	1.0;15;70
IRAS 21419+5832	μ Cep	21:43:30.46106	+58:46:48.1602	s*r	SRC	M2-Ia	12/30/06	14:37:33	F450LP	1710037-001	0.5;15;70
IRAS 21439–0226	EP Aqr	21:46:31.84756	–02:12:45.9306	AB*	SRB	M7-III:	5/19/07	18:02:54	F450LP	1711024-001	1.0;15;70
IRAS 21440+7324	PQ Cep	21:44:28.7910	+73:38:04.901	C*	M	C6-,3e	2/3/07	18:41:33	F450LP	1710036-001	1.0;15;70
IRAS 22017+2806	TW Peg	22:03:59.51379	+28:20:54.2474	AB*	SRB	M6-7III	12/7/06	12:14:54	F450LP	1710054-001	1.0;15;70
IRAS 22035+3506	SV Peg	22:05:42.08385	+35:20:54.5280	AB*	SRB	M7	12/11/06	7:15:54	F450LP	1710012-001	1.0;15;70
IRAS 22145–8041	ϵ Oct	22:20:01.67970	–80:26:23.0947	LP*	SRB	M5III	10/12/06	4:38:33	F450LP	1710048-001	1.0;15;70
IRAS 22196–4612	π^{01} Gru	22:22:44.20571	–45:56:52.6115	S*	SRB	S5,7:	11/11/06	7:21:55	F450LP	1710001-001	0.5;15;70
IRAS 22230–4841	S Gru	22:26:05.47415	–48:26:18.7561	Mi*	M	M8(III)e	11/10/06	8:12:50	F450LP	1710134-001	1.0;15;70
IRAS 22233+3013	RV Peg	22:25:36.81	+30:28:21.3	Mi*	M	M6e	6/12/07	15:16:33	F450LP	1711186-001	1.0;15;70
IRAS 22272+5435	HD 235858	22:29:10.3746	+54:51:06.343	pA*	LB	G5Ia	1/3/07	6:17:54	F450LP	1710157-001	0.5;15;70
IRAS 22315+2418	SS Peg	22:33:58.33174	+24:33:53.9758	Mi*	M	M6.5e:	6/11/07	16:06:33	F450LP	1711199-001	1.0;15;70
IRAS 22396–4708	β Gru	22:42:40.05027	–46:53:04.4752	LP?	LC:	M4.5III	11/14/06	8:07:33	F450LP	1710039-001	0.5;15;70
IRAS 22521+1640	HR Peg	22:54:35.62717	+16:56:30.5959	S*	SRB	S4+/1+	6/12/07	20:18:50	F450LP	1711163-001	2.0;8;70
IRAS 22525–2952	V PsA	22:55:19.690	–29:36:44.82	AB*	SRB	M7/8III	5/24/07	14:10:33	F450LP	1711082-001	1.0;15;70
IRAS 23013+2748	β Peg	23:03:46.45746	+28:04:58.0336	LP*	LB	M2.5II-III	6/20/07	20:31:50	F450LP	1711001-001	1.0;15;70
IRAS 23013+3735	CF And	23:03:43.8122	+37:51:13.648	LP*	LB	M7	6/26/07	19:01:50	F450LP	1711005-001	1.0;15;70
IRAS 23041+1016	R Peg	23:06:39.16689	+10:32:36.0892	Mi*	M	M6-8.5e	6/13/07	19:33:02	F450LP	1711196-001	1.0;15;70
IRAS 23070+0824	57 Peg	23:09:31.45738	+08:40:37.7636	S*	SRA	M4S	6/12/07	22:00:55	F450LP	1711166-001	2.0;8;70
IRAS 23166+1655	RAFGL 3068	23:19:12.607	+17:11:33.13	C*	M	C	6/18/07	23:49:47	F450LP	1711044-001	0.5;15;70
IRAS 23173+2600	W Peg	23:19:50.50149	+26:16:43.6587	Mi*	M	M6.5-7.5e	12/24/06	7:52:50	F450LP	1710027-001	1.0;15;70
IRAS F23234+4215	NGC 7662	23:25:53.6	+42:32:06:	PN	11/26/06	16:35:08	F450LP	1710034-001	0.5;15;70
IRAS 23320+4316	LP And	23:34:27.53	+43:33:01.2	C*	M:	C8,3.5eJ	7/8/07	11:09:45	F450LP	1711261-001	0.5;15;70
IRAS 23412–1533	R Aqr	23:43:49.46201	–15:17:04.1385	Sy*	M	M6.5-8.5e	6/11/07	17:37:30	F450LP	1711095-001	1.0;15;70
IRAS 23416+6130	PZ Cas	23:44:03.28104	+61:47:22.1823	s*r	SRC	M3Ia	1/24/07	0:25:05	F450LP	1710147-001	0.5;15;70
IRAS 23438+0312	19 Psc	23:46:23.51708	+03:29:12.5244	C*	LB	C7,2	6/19/07	18:07:52	F450LP	1711064-001	1.0;15;70
IRAS 23528+4821	RS And	23:55:21.7415	+48:38:17.737	Mi*	SRA	...	1/14/07	5:21:07	F450LP	1710022-001	1.0;15;70
IRAS 23558+5106	R Cas	23:58:24.87336	+51:23:19.7011	Mi*	M	M6.5-9e	1/16/07	10:19:13	F450LP	1710028-001	0.5;15;70
IRAS 23564–5651	S Phe	23:59:04.56942	–56:34:32.2980	LP*	SRB	M5e	11/20/06	7:57:05	F450LP	1710050-001	1.0;15;70

a: IRAS catalog names, unless not observed by IRAS. The leading “R” before the coordinate designation indicates that the entry is taken from the IRAS Point Source Reject Catalog (Beichman et al. 1989), while “F” indicates RAS Faint Source Catalog (Moshir et al. 1990).

b: Simbad Object Type: AB* (AGB star), C* (carbon star), LP* (long period variable), Mi* (Mira), No* (nova), OH* (OH/IR star), pA* (post-AGB star), PN (planetary nebula), RC* (R CrB star), S* (S star), s*r (supergiant star), Sy* (symbiotic star), and SNI (type I supernova). “?” indicates that the type identification is tentative (i.e., a candidate).

c: Variability Type: “:” indicates that the type identification is tentative (i.e., a candidate).

d: Parameters for the FIS01 AOT (Kawada et al. 2007): (reset interval [s]);(scan speed [arcsecs⁻¹]);(shift size [arcsec]).

Table 2. Parameters and Characteristics of FIS Surface
Brightness Correction

Band	Power-Law Fit Parameters		Correction Accuracy (%)	Flux Range (Jy)
	n	c		
N60	0.897±0.009	1.23 ±0.03	97±11	0.14 – 320
WIDE-S	0.875±0.009	1.30 ±0.02	103±11	0.23 – 360
WIDE-L	0.949±0.009	1.16 ±0.02	94±16	0.36 – 270
N160	0.977±0.010	0.462±0.012	97±21	1.7 – 250

Note: The derived (n, c) parameters are valid only when the surface brightness units of the input *AKARI* slow-scan maps are given in MJy sr^{-1} .

Table 3. Measured far-IR flux densities of the MLHES targets

Target Name	N65 (Jy)	WIDE-S (Jy)	WIDE-L (Jy)	N160 (Jy)
IRAS 00042+4248	3.77 ± 0.03(+1) [†]	2.96 ± 0.03(+1) [†]	5.95 ± 0.06(+0)	4.14 ± 0.07(+0)
IRAS 00102+7214	5.32 ± 0.03(+1)	4.72 ± 0.04(+1)	1.08 ± 0.01(+1)	1.15 ± 0.01(+1)
IRAS 00128-3219	3.25 ± 0.04(+0)	2.59 ± 0.04(+0)	3.24 ± 0.11(-1)	...
IRAS 00245-0652	5.84 ± 0.04(+0) [†]	4.88 ± 0.03(+0) [†]	1.23 ± 0.02(+0) [†]	1.57 ± 0.14(-1)
IRAS 00248+3518	3.25 ± 0.04(+0) [†]	3.68 ± 0.06(+0) [†]	1.65 ± 0.04(+0)	1.23 ± 0.08(+0)*
IRAS 00254-3317	7.03 ± 0.15(-1)	4.96 ± 0.11(-1)	2.70 ± 1.56(-3)	...
IRAS 01037+1219	1.62 ± 0.01(+2)	1.30 ± 0.02(+2)	2.35 ± 0.01(+1)	2.13 ± 0.01(+1)
IRAS 01144+6658	5.96 ± 0.05(+1)	4.00 ± 0.05(+1)	3.13 ± 0.07(+0)	1.79 ± 0.08(+0)
IRAS 01246-3248	3.61 ± 0.02(+1)	3.09 ± 0.03(+1)	6.52 ± 0.04(+0)	3.37 ± 0.05(+0)
IRAS 01556+4511	2.71 ± 0.02(+1)	2.16 ± 0.02(+1)	5.40 ± 0.06(+0)	2.15 ± 0.05(+0)
IRAS 02143+4404	7.16 ± 0.05(+0)	5.46 ± 0.04(+0)	6.16 ± 0.14(-1)	9.83 ± 1.36(-2)
IRAS 02168-0312	1.88 ± 0.01(+2)	1.51 ± 0.02(+2)	2.85 ± 0.01(+1)	2.43 ± 0.01(+1)
IRAS 02302+4525	7.47 ± 0.05(+0)	5.95 ± 0.04(+0)	1.37 ± 0.02(+0)	6.37 ± 0.30(-1)
IRAS 02427-5430	4.35 ± 0.04(+0)	3.67 ± 0.03(+0)	3.78 ± 0.16(-1)	...
IRAS 02464-5915	2.57 ± 0.06(+0)	1.68 ± 0.02(+0)	1.54 ± 0.10(-1)	...
IRAS 02522-5005	4.29 ± 0.03(+1)	3.54 ± 0.03(+1)	6.76 ± 0.06(+0)	5.47 ± 0.11(+0)
IRAS 03019+3838	6.74 ± 0.06(+0) [†]	4.77 ± 0.05(+0) [†]	3.16 ± 0.18(-1)	...
IRAS 03062+6107	1.03 ± 0.01(+1)	1.01 ± 0.02(+1) [†]	5.83 ± 0.54(+0)* [†]	1.03 ± 0.09(+1)* [†]
IRAS 03112-5730	3.63 ± 0.05(+0) [†]	2.96 ± 0.04(+0)	1.96 ± 0.13(-1)	...
IRAS 03172-2156	2.71 ± 0.04(+0)	1.91 ± 0.04(+0) [†]	1.45 ± 0.10(-1)	1.03 ± 0.12(-1)
GK Per
IRAS 03374+6229	1.00 ± 0.01(+1)	7.40 ± 0.14(+0)	1.43 ± 0.32(+0)*	...
IRAS 03463-0710	2.50 ± 0.02(+0)	3.57 ± 0.02(+0)	1.20 ± 0.03(+0)	1.40 ± 0.05(+0)*
IRAS 04020-1551	1.24 ± 0.01(+1) [†]	9.96 ± 0.08(+0) [†]	1.71 ± 0.02(+0) [†]	3.81 ± 0.22(-1)
IRAS 04330-6307	1.08 ± 0.02(+0)	9.32 ± 0.10(-1)	4.11 ± 0.46(-2)	...
IRAS 04361-6210	2.45 ± 0.02(+2)	1.84 ± 0.02(+2)	2.99 ± 0.01(+1)	2.13 ± 0.02(+1)
IRAS 04387-3819	5.31 ± 0.04(+0)	3.92 ± 0.03(+0) [†]	4.07 ± 0.15(-1)	...
IRAS 04459+6804	5.24 ± 0.05(+0)	4.69 ± 0.05(+0)	4.69 ± 0.29(-1)	...
IRAS 04573-1452	1.54 ± 0.01(+1)	1.22 ± 0.01(+1)	2.50 ± 0.05(+0)	6.26 ± 0.38(-1)
IRAS 05071-6327	6.05 ± 0.19(-1)	3.45 ± 0.13(-1)
IRAS 05096-4834	6.89 ± 0.05(+0) [†]	5.44 ± 0.04(+0) [†]	1.01 ± 0.02(+0) [†]	1.75 ± 0.18(-1)
IRAS 05411-8625	4.42 ± 0.05(+0) [†]	2.89 ± 0.03(+0) [†]	5.50 ± 0.29(-1)	...
IRAS 05251-1244	7.81 ± 0.05(+1)	5.77 ± 0.06(+1)	7.91 ± 0.08(+0)	6.20 ± 0.10(+0)
IRAS 05418-4628	3.36 ± 0.04(+0) [†]	4.09 ± 0.03(+0) [†]	1.20 ± 0.03(+0) [†]	...
IRAS 05524+0723	3.88 ± 0.02(+2) [†]	2.81 ± 0.02(+2) [†]	3.18 ± 0.03(+1)	1.86 ± 0.02(+1) [†]
IRAS 05528+2010	3.41 ± 0.04(+1)	2.49 ± 0.05(+1)	3.48 ± 0.21(+0)	1.81 ± 0.17(+0)
IRAS 06176-1036	1.43 ± 0.01(+2)	1.05 ± 0.02(+2)	1.55 ± 0.02(+1)	9.69 ± 0.16(+0)
IRAS 07059-5818	3.47 ± 0.16(-1)	1.66 ± 0.12(-1)
IRAS 07245+4605	6.77 ± 0.10(+0)	6.67 ± 0.11(+0) [†]	7.23 ± 0.38(-1)	7.33 ± 1.14(-2)
IRAS 08349-5945	5.70 ± 0.07(+0)	1.20 ± 0.02(+1)	2.92 ± 0.03(+1)	3.14 ± 0.45(-1)
IRAS 09200-5805	8.82 ± 0.09(+0)	7.89 ± 0.14(+0)	6.28 ± 0.70(-1)	5.70 ± 0.84(-1)
IRAS 09429-2148	4.44 ± 0.04(+1)	3.25 ± 0.04(+1)	4.38 ± 0.04(+0)	2.03 ± 0.04(+0)
IRAS 09452+1330	2.43 ± 0.01(+3)	2.34 ± 0.02(+3)	4.61 ± 0.01(+2)	4.75 ± 0.01(+2)
Y Hya	5.11 ± 0.07(+0)	5.23 ± 0.09(+0)	9.27 ± 0.44(-1)	8.85 ± 0.57(-1)*
IRAS 10223-1823	4.16 ± 0.02(+1) [†]	4.86 ± 0.04(+1) [†]	5.83 ± 0.04(+0) [†]	3.61 ± 0.09(+0)* [†]
IRAS 10323-4611	2.99 ± 0.03(+1)	2.25 ± 0.03(+1)	1.84 ± 0.06(+0)	9.91 ± 0.48(-1)
IRAS 10329-3918	3.13 ± 0.01(+1)	3.21 ± 0.01(+1)	1.26 ± 0.01(+1)	4.97 ± 0.07(+0)
IRAS 10350-1307	3.44 ± 0.02(+1)	3.63 ± 0.02(+1)	1.47 ± 0.01(+1)	9.94 ± 0.12(+0)
IRAS 10416+6740	4.14 ± 0.04(+0)	4.58 ± 0.04(+0)	1.52 ± 0.03(+0) [†]	1.08 ± 0.16(-1)
IRAS 10580-1803	3.77 ± 0.03(+1)	3.37 ± 0.03(+1)	9.55 ± 0.08(+0)	7.52 ± 0.13(+0)*
IRAS 11119+5517	1.21 ± 0.03(+0)	7.41 ± 0.05(+0) [†]	9.43 ± 0.24(-1)	1.30 ± 0.07(+0)*
IRAS 11125+7524	3.94 ± 0.04(+0)	3.00 ± 0.03(+0)	3.81 ± 0.21(-1)	...
IRAS 11251+4527	1.47 ± 0.02(+0)	1.00 ± 0.01(+0)
IRAS 11385-5517	1.92 ± 0.02(+2)	1.70 ± 0.03(+2)	3.98 ± 0.03(+1)	3.80 ± 0.04(+1)
IRAS 11461-3542	2.03 ± 0.02(+1)	1.89 ± 0.02(+1)	5.48 ± 0.13(+0)	1.98 ± 0.08(+0)
IRAS 11538+5808	1.64 ± 0.02(+0)	1.07 ± 0.02(+0)	1.59 ± 0.37(-2)	...
IRAS 12380+5607	1.06 ± 0.01(+1)	9.17 ± 0.06(+0)	2.48 ± 0.04(+0)	1.75 ± 0.10(+0)*
IRAS 12427+4542	1.50 ± 0.01(+1)	1.59 ± 0.01(+1)	3.56 ± 0.05(+0)	1.45 ± 0.13(+0)*
IRAS 12526+4728	9.13 ± 0.17(-1)	6.71 ± 0.13(-1)	1.56 ± 0.14(-1)	...
IRAS 12544+6615	5.06 ± 0.05(+0)	5.90 ± 0.04(+0)	1.99 ± 0.03(+0)	...
IRAS 13001+0527	2.65 ± 0.02(+1)	2.20 ± 0.02(+1)	4.99 ± 0.04(+0)	1.79 ± 0.04(+0)
IRAS 13172+4547	1.92 ± 0.02(+0) [†]	1.43 ± 0.02(+0)	1.50 ± 0.09(-1)	1.69 ± 0.17(-1)
IRAS F13370-3123	2.62 ± 0.02(+1)	3.34 ± 0.03(+1) [†]	1.58 ± 0.01(+1) [†]	1.54 ± 0.01(+1) [†]
IRAS 13468+3947	2.78 ± 0.03(+0) [†]	1.79 ± 0.02(+0) [†]	1.86 ± 0.11(-1)	...
IRAS 13462-2807	1.99 ± 0.01(+2)	1.71 ± 0.02(+2)	3.98 ± 0.02(+1)	2.80 ± 0.02(+1)
IRAS 14003-7633	3.78 ± 0.02(+1)	3.04 ± 0.03(+1) [†]	5.44 ± 0.08(+0)	4.35 ± 0.10(+0)
IRAS 14162+6701	1.33 ± 0.02(+0)	8.94 ± 0.08(-1)
IRAS 14219+2555	5.28 ± 0.03(+1)	4.22 ± 0.04(+1)	7.74 ± 0.04(+0)	4.39 ± 0.06(+0)
IRAS 14277+3904	1.07 ± 0.03(+0)	4.96 ± 0.15(-1)
IRAS 14567+6607	2.79 ± 0.04(+0)	1.66 ± 0.02(+0) [†]	1.39 ± 0.11(-1)	...
IRAS 14591-4438	1.16 ± 0.01(+1)	8.37 ± 0.13(+0)	1.13 ± 0.06(+0)	6.62 ± 0.62(-1)
IRAS 15094-6953	1.34 ± 0.01(+1)	1.31 ± 0.01(+1)	5.03 ± 0.08(+0)	4.35 ± 0.16(+0)*
IRAS 15255+1944	5.55 ± 0.06(+0)	4.16 ± 0.06(+0)	7.98 ± 0.37(-1)	...
IRAS 15396+3842	5.50 ± 0.11(-1)	4.77 ± 0.09(-1)	1.01 ± 0.30(-2)	...
IRAS 15465+2818	2.16 ± 0.04(+0)	3.80 ± 0.07(+0)	2.80 ± 0.08(+0)*	7.25 ± 0.54(-1)*
IRAS 15477+3943	2.54 ± 0.02(+0)	1.82 ± 0.02(+0)	2.34 ± 0.09(-1)	...

Table 3. (Continued)

Target Name	N65	WIDE-S	WIDE-L	N160
IRAS 15492+4837	1.03 ± 0.01(+1)	8.47 ± 0.06(+0) [†]	9.32 ± 0.24(-1)	...
IRAS 16011+4722	2.59 ± 0.02(+1) [†]	2.24 ± 0.02(+1) [†]	3.81 ± 0.03(+0) [†]	2.47 ± 0.06(+0) [†]
IRAS 16164+5952	9.23 ± 0.15(-1)	5.41 ± 0.07(-1) [†]
IRAS 16255+2801	6.73 ± 0.17(-1)	1.05 ± 0.02(+0)	5.27 ± 0.34(-1)*	...
IRAS 16306+7223	4.43 ± 0.05(+0)	3.14 ± 0.04(+0)	6.75 ± 0.29(-1) [†]	...
IRAS 16418+5459	6.62 ± 0.06(+0)	6.42 ± 0.05(+0)	9.60 ± 0.20(-1)	...
IRAS 16457+4219	5.11 ± 0.10(-1)	3.57 ± 0.08(-1) [†]
IRAS 16473+5753	1.71 ± 0.02(+0)	1.30 ± 0.01(+0)	1.21 ± 0.10(-1)	6.56 ± 1.29(-2)
IRAS 17028-1004	1.23 ± 0.01(+2)	1.14 ± 0.01(+2)	3.12 ± 0.04(+1)	2.49 ± 0.04(+1) [†]
IRAS 17081+6422	2.36 ± 0.04(+0)	1.92 ± 0.03(+0)	2.92 ± 0.16(-1)	2.66 ± 0.23(-1)
IRAS 17119+0859	2.00 ± 0.02(+1) [†]	1.37 ± 0.01(+1) [†]	1.27 ± 0.03(+0)	4.99 ± 0.32(-1)
IRAS 17389-5742	7.27 ± 0.06(+0)	6.90 ± 0.10(+0) [†]	7.33 ± 0.32(-1)	...
IRAS 17584+6638A	1.14 ± 0.01(+2)	1.01 ± 0.01(+2)	1.76 ± 0.01(+1)	1.32 ± 0.02(+1)*
IRAS 18216+6419	1.39 ± 0.02(+0)	1.38 ± 0.02(+0)	3.84 ± 0.16(-1)	4.43 ± 0.52(-1)*
IRAS 18517+3257	4.82 ± 0.02(+1) [†]	7.56 ± 0.05(+1) [†]	2.90 ± 0.01(+1) [†]	2.94 ± 0.02(+1)
IRAS 18527+3650	4.40 ± 0.03(+0) [†]	6.74 ± 0.03(+0) [†]	1.98 ± 0.03(+0)	8.74 ± 1.00(-2)
IRAS 18537+4352	1.75 ± 0.01(+1)	1.87 ± 0.01(+1)	3.90 ± 0.04(+0)	2.64 ± 0.10(+0)*
IRAS 19143-5032	6.28 ± 0.07(+0)	5.40 ± 0.07(+0)	6.82 ± 0.29(-1) [†]	4.19 ± 0.54(-1) [†] *
IRAS 19233+7627	3.96 ± 0.09(+0)	4.29 ± 0.02(+0)	1.76 ± 0.03(+0)	...
IRAS 19314-1629	4.54 ± 0.06(+0)	5.81 ± 0.11(+0)	2.92 ± 0.06(+0)	1.75 ± 0.09(+0)*
IRAS 19354+5005	9.13 ± 0.07(+0)	7.64 ± 0.08(+0)	1.34 ± 0.04(+0)	1.63 ± 0.08(+0)*
IRAS 19390+3229	2.39 ± 0.05(+0)	2.15 ± 0.09(+0)	9.01 ± 1.56(-1)*	... cln
IRAS 19409+5520	6.15 ± 0.15(-1)	3.17 ± 0.11(-1)
IRAS 19434+5024	2.93 ± 0.01(+1)	3.12 ± 0.03(+1)	4.03 ± 0.06(+0)	2.09 ± 0.07(+0)
IRAS 19510-5919	1.90 ± 0.01(+1)	1.67 ± 0.01(+1)	3.11 ± 0.04(+0)	7.30 ± 0.32(-1)
IRAS 19574+2234	1.10 ± 0.00(+2)	2.26 ± 0.01(+2)	8.13 ± 0.08(+1)	1.57 ± 0.01(+2)
IRAS 19575-5930	5.36 ± 0.07(+0)	3.60 ± 0.06(+0)	4.27 ± 0.21(-1)	...
IRAS 20038-2722	2.21 ± 0.02(+1)	1.89 ± 0.02(+1)	5.30 ± 0.09(+0)	4.15 ± 0.10(+0)*
IRAS 20088+4618	6.17 ± 0.08(+0)	5.29 ± 0.14(+0)	6.00 ± 2.12(-1)*	... cln
IRAS 20075-6005	3.63 ± 0.02(+1)	2.99 ± 0.02(+1)	9.94 ± 0.06(+0)	3.92 ± 0.09(+0)
IRAS 20120-4433	9.67 ± 0.08(+0)	1.89 ± 0.01(+1)	3.07 ± 0.01(+1)	2.62 ± 0.02(+1)
IRAS 20141-2128	3.99 ± 0.09(+0)	4.54 ± 0.11(+0)	1.05 ± 0.05(+0)	9.52 ± 0.67(-1)*
IRAS 20248-2825	2.41 ± 0.02(+1)	1.97 ± 0.02(+1)	3.51 ± 0.06(+0)	2.89 ± 0.12(+0)*
IRAS 20396+4757	4.06 ± 0.03(+1)	2.58 ± 0.03(+1)	5.69 ± 0.41(+0)*	1.59 ± 0.16(+0)*
AFGL 2688	1.92 ± 0.01(+3)	1.88 ± 0.02(+3)	4.56 ± 0.02(+2)	4.01 ± 0.02(+2)
NGC 7027	6.01 ± 0.04(+2)	5.54 ± 0.08(+2)	8.57 ± 0.06(+1)	8.21 ± 0.09(+1)
IRAS 21197-6956	3.95 ± 0.06(+0) [†]	3.47 ± 0.05(+0) [†]	5.83 ± 0.24(-1) [†]	...
IRAS 21282+5050	2.20 ± 0.02(+1)	1.52 ± 0.03(+1)	2.30 ± 0.59(+0)*	1.05 ± 0.36(+0)*
IRAS 21358+7823	1.61 ± 0.01(+1)	1.41 ± 0.01(+1)	2.94 ± 0.04(+0)	1.79 ± 0.05(+0)
IRAS 21412+3747	1.08 ± 0.01(+1)	1.41 ± 0.01(+1)	5.71 ± 0.13(+0)	4.66 ± 0.17(+0)*
IRAS 21419+5832	1.66 ± 0.01(+2) [†]	1.14 ± 0.01(+2) [†]	2.32 ± 0.12(+1) [†] *	2.80 ± 0.14(+1) [†] *
IRAS 21440+7324	5.17 ± 0.04(+0)	4.32 ± 0.03(+0) [†]	3.62 ± 0.13(+0) [†] *	9.27 ± 0.53(-1) [†] *
IRAS 21439-0226	3.15 ± 0.02(+1)	2.62 ± 0.02(+1)	4.51 ± 0.03(+0)	3.42 ± 0.06(+0)*
IRAS 22017+2806	1.42 ± 0.01(+1)	1.26 ± 0.01(+1)	2.75 ± 0.04(+0)	1.06 ± 0.03(+0)
IRAS 22035+3506	1.62 ± 0.01(+1)	1.41 ± 0.01(+1) [†]	2.72 ± 0.05(+0) [†]	2.74 ± 0.11(+0) [†] *
IRAS 22145-8041	2.90 ± 0.04(+0)	1.88 ± 0.04(+0) [†]	2.34 ± 0.31(-1)	...
IRAS 22196-4612	5.41 ± 0.03(+1)	4.21 ± 0.04(+1)	5.69 ± 0.05(+0)	3.17 ± 0.07(+0)
IRAS 22233+3013	5.55 ± 0.04(+0)	4.09 ± 0.03(+0)	3.81 ± 0.13(-1)	4.77 ± 0.22(-1)
IRAS 22230-4841	3.48 ± 0.04(+0)	2.47 ± 0.03(+0) [†]	3.90 ± 0.14(-1)	...
IRAS 22272+5435	1.45 ± 0.01(+2)	2.51 ± 0.02(+2)	2.90 ± 0.02(+2)	5.35 ± 0.03(+2)
IRAS 22315+2418	2.17 ± 0.03(+0)	1.89 ± 0.03(+0)	3.81 ± 0.16(-1)	...
IRAS 22396-4708	2.27 ± 0.02(+1)	1.74 ± 0.02(+1)	2.98 ± 0.03(+0)	2.77 ± 0.09(+0)*
IRAS 22521+1640	5.76 ± 0.16(-1)	4.03 ± 0.16(-1)
IRAS 22525-2952	1.07 ± 0.01(+1)	8.37 ± 0.08(+0)	1.11 ± 0.02(+0)	2.44 ± 0.20(-1)
IRAS 23013+3735	3.85 ± 0.03(+0) [†]	2.76 ± 0.02(+0) [†]	1.36 ± 0.05(+0) [†] *	2.21 ± 0.08(+0) [†] *
IRAS 23013+2748	8.03 ± 0.07(+0)	5.84 ± 0.06(+0)	1.40 ± 0.05(+0)*	6.50 ± 0.30(-1)*
IRAS 23041+1016	4.76 ± 0.04(+0)	3.57 ± 0.03(+0)	5.05 ± 0.15(-1)	1.06 ± 0.11(-1)
IRAS 23070+0824	1.46 ± 0.03(+0)	1.02 ± 0.02(+0)	5.60 ± 0.76(-2)	...
IRAS 23166+1655	2.62 ± 0.02(+2)	2.04 ± 0.03(+2)	2.60 ± 0.01(+1)	2.22 ± 0.01(+1) [†]
IRAS 23173+2600	6.17 ± 0.07(+0)	5.86 ± 0.10(+0) [†]	6.63 ± 0.33(-1)	...
IRAS F23234+4215	2.11 ± 0.01(+1)	2.07 ± 0.02(+1)	2.01 ± 0.04(+0)	1.25 ± 0.06(+0)
IRAS 23320+4316	1.14 ± 0.01(+2)	7.92 ± 0.10(+1)	9.98 ± 0.07(+0)	8.05 ± 0.11(+0)
IRAS 23412-1533	2.52 ± 0.02(+1)	1.83 ± 0.02(+1)	2.85 ± 0.02(+0)	2.90 ± 0.06(+0)*
IRAS 23416+6130	8.44 ± 0.06(+1)	7.31 ± 0.28(+1)	3.89 ± 0.05(+1)	4.39 ± 0.08(+1)*
IRAS 23438+0312	9.63 ± 0.05(+0)	8.28 ± 0.05(+0)	2.53 ± 0.03(+0) [†]	2.07 ± 0.07(+0) [†] *
IRAS 23528+4821	5.25 ± 0.04(+0)	6.22 ± 0.03(+0)	1.04 ± 0.02(+0)	...
IRAS 23558+5106	1.05 ± 0.01(+2)	8.86 ± 0.08(+1)	3.28 ± 0.03(+1)	3.08 ± 0.03(+1)*
IRAS 23564-5651	2.52 ± 0.03(+0)	2.03 ± 0.02(+0)	2.59 ± 0.13(-1)	...

Note - *: the source boundary adopted from a shorter waveband; †: the source boundary is manually adjusted to remove unwanted regions.

Table 4. The far-IR sky surface brightnesses at the position of the MLHES targets in the Galactic coordinates

Target Name ^a	Gal. Coord.		N65	WIDE-S	WIDE-L	N160
	<i>l</i> (J2000)	<i>b</i> (J2000)	(MJy sr ⁻¹)	(MJy sr ⁻¹)	(MJy sr ⁻¹)	(MJy sr ⁻¹)
IRAS 17028-1004	10.8987	+18.0567	4.79±0.68(+0)	1.35±0.06(+1)	3.74±0.47(+1)	5.90±0.95(+1)
IRAS 20038-2722	14.7707	-27.6822	2.76±0.42(+0)	4.21±0.40(+0)	7.08±1.57(+0)	1.09±0.48(+1)
IRAS 20248-2825	15.1857	-32.4288	2.27±0.39(+0)	3.40±0.26(+0)	4.88±1.28(+0)	7.07±3.63(+0)
IRAS 22525-2952	20.4814	-64.4047	1.29±0.31(+0)	1.58±0.18(+0)	1.44±0.69(+0)	3.44±2.31(+0)
IRAS 20141-2128	21.941	-27.9385	3.04±0.33(+0)	4.30±0.33(+0)	7.42±1.11(+0)	1.20±0.40(+1)
IRAS 19314-1629	22.7377	-16.7008	3.42±0.34(+0)	5.72±0.36(+0)	1.11±0.20(+1)	1.71±0.46(+1)
IRAS 15255+1944	29.515	+53.4767	1.68±0.26(+0)	2.72±0.27(+0)	5.36±1.30(+0)	9.12±2.26(+0)
IRAS 17119+0859	29.9424	+25.6156	2.11±0.31(+0)	4.17±0.30(+0)	9.89±1.31(+0)	1.63±0.34(+1)
IRAS 14219+2555	34.2773	+69.2128	1.16±0.29(+0)	1.42±0.20(+0)	2.49±0.60(+0)	5.50±1.81(+0)
IRAS 15465+2818	45.0496	+50.9782	9.52±1.97(-1)	1.59±0.13(+0)	3.45±0.64(+0)	6.02±1.64(+0)
IRAS 16255+2801	47.0517	+42.4826	1.61±0.27(+0)	2.66±0.30(+0)	5.21±1.21(+0)	9.32±2.77(+0)
IRAS 21439-0226	54.1999	-39.2604	1.80±0.26(+0)	2.16±0.19(+0)	3.61±0.90(+0)	5.41±2.62(+0)
IRAS 19574+2234	60.836	-3.6961	9.21±0.65(+0)	2.86±0.25(+1)	7.25±0.79(+1)	1.12±0.14(+2)
IRAS 15396+3842	61.8484	+52.8757	1.32±0.36(+0)	1.38±0.32(+0)	1.97±0.75(+0)	4.97±1.59(+0)
IRAS 18517+3257	63.1701	+13.9781	1.81±0.29(+0)	3.31±0.31(+0)	6.95±1.09(+0)	1.32±0.35(+1)
IRAS 15477+3943	63.2731	+51.2253	1.24±0.43(+0)	1.46±0.34(+0)	2.16±0.72(+0)	5.41±2.43(+0)
IRAS 23412-1533	66.5168	-70.3255	1.49±0.26(+0)	1.56±0.15(+0)	1.56±0.84(+0)	2.39±1.77(+0)
IRAS 16457+4219	66.7042	+40.2520	1.09±0.31(+0)	1.39±0.22(+0)	1.99±0.49(+0)	5.05±1.91(+0)
IRAS 18527+3650	66.9257	+15.3223	1.47±0.27(+0)	2.95±0.22(+0)	6.90±0.97(+0)	1.31±0.41(+1)
IRAS 19390+3229	67.2727	+4.8820	7.72±0.45(+0)	1.87±0.08(+1)	3.44±0.63(+1)	5.49±1.23(+1)
IRAS 14277+3904	68.9559	+66.3926	1.58±0.42(+0)	1.43±0.35(+0)	1.83±0.60(+0)	3.59±1.91(+0)
IRAS 18537+4352	73.8151	+17.7912	1.75±0.23(+0)	3.26±0.36(+0)	6.22±1.31(+0)	1.22±0.26(+1)
IRAS 16011+4722	74.464	+47.7854	8.17±2.65(-1)	1.07±0.11(+0)	2.75±0.61(+0)	6.26±1.50(+0)
IRAS 15492+4837	76.9789	+49.4432	9.36±2.36(-1)	1.21±0.17(+0)	2.61±0.75(+0)	5.51±1.61(+0)
AFGL 2688	80.1677	-6.5032	5.43±1.11(+0)	1.35±0.16(+1)	2.69±0.52(+1)	4.57±0.71(+1)
IRAS 20088+4618	82.1356	+7.0936	1.99±0.27(+1)	4.35±0.49(+1)	8.80±1.16(+1)	1.43±0.16(+2)
IRAS 13468+3947	82.6559	+72.7697	1.97±0.65(+0)	1.85±0.55(+0)	2.11±0.71(+0)	4.81±1.98(+0)
IRAS 19354+5005	82.6756	+13.7829	1.91±0.27(+0)	3.63±0.31(+0)	7.87±1.68(+0)	1.37±0.29(+1)
IRAS 16418+5459	83.3407	+40.1805	7.85±2.61(-1)	1.02±0.16(+0)	2.30±0.66(+0)	5.54±2.19(+0)
IRAS 19434+5024	83.5618	+12.7922	1.88±0.35(+0)	4.79±0.29(+0)	9.53±1.55(+0)	1.92±0.37(+1)
IRAS 22017+2806	83.7849	-21.5198	2.82±0.49(+0)	5.03±0.44(+0)	6.93±1.25(+0)	1.29±0.32(+1)
IRAS 23070+0824	84.7733	-46.5059	1.97±0.14(+0)	2.31±0.18(+0)	3.09±1.04(+0)	5.12±3.18(+0)
NGC 7027	84.9298	-3.4961	1.63±0.15(+1)	4.50±0.37(+1)	1.07±0.11(+2)	1.75±0.26(+2)
IRAS 23041+1016	85.4073	-44.5601	1.66±0.26(+0)	2.34±0.22(+0)	4.12±1.18(+0)	7.11±2.23(+0)
IRAS 20396+4757	86.5362	+3.7667	2.14±0.20(+1)	6.18±0.42(+1)	1.60±0.19(+2)	2.47±0.22(+2)
IRAS 22521+1640	86.8259	-37.6054	2.19±0.19(+0)	3.48±0.19(+0)	6.01±1.47(+0)	1.04±0.38(+1)
IRAS 16473+5753	86.8912	+38.9458	2.48±0.63(+0)	2.43±0.45(+0)	2.77±0.84(+0)	6.03±2.73(+0)
IRAS 21412+3747	86.9105	-11.3599	5.33±0.66(+0)	1.11±0.07(+1)	1.98±0.33(+1)	3.33±1.15(+1)
IRAS 22315+2418	87.1501	-28.5927	1.13±0.17(+0)	1.78±0.14(+0)	3.74±0.96(+0)	7.08±1.96(+0)
IRAS 19409+5520	87.925	+15.3704	2.60±0.39(+0)	4.88±0.24(+0)	9.80±1.78(+0)	1.97±0.69(+1)
IRAS 22035+3506	88.7152	-16.2856	2.56±0.22(+0)	5.50±0.27(+0)	1.12±0.21(+1)	2.00±0.49(+1)
IRAS 22233+3013	89.2141	-22.6878	1.50±0.28(+0)	2.56±0.11(+0)	5.33±1.23(+0)	9.49±3.11(+0)
IRAS 16164+5952	90.7378	+42.3190	3.80±0.85(+0)	3.19±0.56(+0)	3.14±0.77(+0)	7.38±2.41(+0)
IRAS 23438+0312	93.2841	-55.5955	2.22±0.37(+0)	2.59±0.18(+0)	3.83±1.22(+0)	6.79±3.04(+0)
IRAS 23166+1655	93.5267	-40.3539	1.13±0.47(+0)	1.81±0.87(+0)	2.85±0.87(+0)	5.40±2.33(+0)
IRAS 21282+5050	93.9871	-0.1178	2.08±0.16(+1)	6.03±0.34(+1)	1.65±0.17(+2)	2.61±0.20(+2)
IRAS 18216+6419	94.0257	+27.4283	1.37±0.33(+0)	2.05±0.27(+0)	4.06±0.85(+0)	7.80±3.14(+0)
IRAS 17081+6422	94.3434	+35.3483	3.80±0.49(+0)	3.62±0.30(+0)	3.48±0.86(+0)	7.20±3.09(+0)
IRAS 23013+2748	95.7486	-29.0449	1.83±0.28(+0)	3.08±0.36(+0)	6.68±1.51(+0)	1.29±0.35(+1)
IRAS 17584+6638A	96.4682	+29.9545	1.05±0.44(+0)	1.87±0.22(+0)	4.10±0.76(+0)	8.23±2.73(+0)
IRAS 23173+2600	98.5749	-32.2244	1.64±0.23(+0)	2.91±0.26(+0)	5.94±0.97(+0)	1.01±0.29(+1)
IRAS 23013+3735	100.5232	-20.2866	2.32±0.24(+0)	5.69±0.31(+0)	1.27±0.19(+1)	2.39±0.56(+1)
IRAS 21419+5832	100.5953	+4.3149	2.13±0.32(+1)	5.98±1.19(+1)	1.08±0.11(+2)	1.61±0.22(+2)
IRAS 22272+5435	103.349	-2.5181	1.34±0.15(+1)	3.52±0.34(+1)	7.52±1.10(+1)	1.18±0.21(+2)
IRAS 14567+6607	104.8714	+46.5260	3.29±0.71(+0)	3.10±0.44(+0)	3.11±0.82(+0)	7.65±2.38(+0)
IRAS 16306+7223	105.0108	+36.2380	1.40±0.36(+0)	2.49±0.19(+0)	4.26±1.03(+0)	8.03±2.34(+0)
IRAS 00245-0652	106.105	-68.6779	2.06±0.26(+0)	2.32±0.22(+0)	2.80±0.94(+0)	3.58±2.96(+0)
IRAS F23234+4215	106.5598	-17.6011	1.68±0.36(+0)	3.81±0.35(+0)	9.45±1.67(+0)	1.59±0.46(+1)
IRAS 13172+4547	107.8914	+70.7739	2.35±0.78(+0)	2.52±0.57(+0)	3.32±0.91(+0)	7.10±3.10(+0)
IRAS 19233+7627	108.2509	+24.6048	1.27±0.23(+0)	2.35±0.20(+0)	7.32±1.10(+0)	1.37±0.32(+1)
IRAS 23320+4316	108.455	-17.1467	1.90±0.45(+0)	3.97±0.29(+0)	9.57±1.81(+0)	1.78±0.52(+1)
IRAS 14162+6701	110.4345	+48.1966	2.48±0.41(+0)	2.55±0.29(+0)	3.08±0.89(+0)	6.65±2.78(+0)
IRAS 21440+7324	110.6427	+15.4053	2.90±0.44(+0)	7.86±0.56(+0)	2.62±0.33(+1)	4.79±0.93(+1)
IRAS 23528+4821	113.4682	-13.2004	1.96±0.30(+0)	3.94±0.35(+0)	9.10±1.61(+0)	1.71±0.46(+1)
IRAS 21358+7823	113.8444	+19.3897	1.48±0.29(+0)	3.61±0.34(+0)	1.15±0.16(+1)	2.17±0.50(+1)
IRAS 00042+4248	114.3475	-19.0445	1.42±0.23(+0)	2.66±0.20(+0)	5.92±1.09(+0)	1.14±0.31(+1)
IRAS 23558+5106	114.5609	-10.6191	2.39±0.46(+0)	5.59±0.34(+0)	1.60±0.26(+1)	2.60±0.48(+1)
IRAS 23416+6130	115.0582	-0.0478	1.39±0.11(+1)	3.87±0.19(+1)	9.78±0.93(+1)	1.69±0.27(+2)
IRAS 00248+3518	117.4764	-27.0310	1.42±0.32(+0)	2.53±0.17(+0)	5.08±1.13(+0)	9.19±3.47(+0)
IRAS 00102+7214	120.0162	+9.8681	2.90±0.34(+0)	7.00±0.38(+0)	2.02±0.31(+1)	3.31±0.99(+1)
IRAS 12526+4728	121.198	+69.9197	2.31±0.70(+0)	2.05±0.50(+0)	1.73±0.83(+0)	3.86±2.12(+0)
IRAS 12544+6615	122.1227	+51.1260	9.18±2.51(-1)	1.17±0.19(+0)	2.84±0.64(+0)	6.47±2.25(+0)
IRAS 01144+6658	125.4913	+4.4917	5.74±0.54(+0)	1.79±0.07(+1)	6.07±0.35(+1)	1.06±0.20(+2)
IRAS 12380+5607	126.1625	+61.2121	8.68±2.74(-1)	9.48±1.71(-1)	2.15±0.62(+0)	5.91±1.60(+0)
IRAS 12427+4542	126.4474	+71.6449	1.10±0.28(+0)	1.45±0.19(+0)	2.82±0.74(+0)	8.29±3.56(+0)
IRAS 01037+1219	128.6417	-50.1074	1.80±0.42(+0)	2.75±0.36(+0)	4.05±1.08(+0)	5.47±2.86(+0)
IRAS 11125+7524	130.7762	+40.4972	9.56±2.75(-1)	1.54±0.12(+0)	3.71±1.02(+0)	8.39±2.55(+0)
IRAS 01556+4511	135.1203	-15.8378	1.96±0.28(+0)	3.44±0.39(+0)	7.21±1.58(+0)	1.34±0.41(+1)
IRAS 11538+5808	136.6269	+57.7722	1.94±0.38(+0)	2.12±0.35(+0)	2.26±0.66(+0)	4.30±2.32(+0)

Table 4. (Continued)

Target Name	$l(J2000)$	$b(J2000)$	N65	WIDE-S	WIDE-L	N160
IRAS 02143+4404	138.7779	-15.9012	1.83±0.22(+0)	3.08±0.22(+0)	6.57±1.49(+0)	1.20±0.40(+1)
IRAS 03062+6107	138.8168	+2.8045	1.02±0.06(+1)	2.75±0.15(+1)	6.96±0.90(+1)	1.19±0.16(+2)
IRAS 10416+6740	139.5893	+45.4140	7.22±1.73(-1)	9.04±1.34(-1)	2.33±0.45(+0)	7.06±2.48(+0)
IRAS 02302+4525	140.9753	-13.6121	1.78±0.23(+0)	3.51±0.27(+0)	7.35±1.24(+0)	1.30±0.44(+1)
IRAS 03374+6229	141.1499	+5.9679	5.91±0.67(+0)	1.70±0.15(+1)	4.94±0.63(+1)	8.92±2.20(+1)
IRAS 04459+6804	142.3897	+14.9236	1.96±0.29(+0)	4.80±0.29(+0)	1.18±0.20(+1)	2.20±0.43(+1)
IRAS 11119+5517	148.4895	+57.0500	1.28±0.56(+0)	1.16±0.36(+0)	1.55±0.80(+0)	3.49±1.65(+0)
IRAS 03019+3838	149.5981	-17.0090	2.33±0.30(+0)	4.28±0.53(+0)	9.53±1.85(+0)	1.84±0.50(+1)
GK Per	150.9553	-10.1042	3.52±0.32(+0)	8.28±0.54(+0)	2.08±0.18(+1)	3.39±0.53(+1)
IRAS 11251+4527	160.1436	+65.4334	2.11±0.61(+0)	1.74±0.44(+0)	1.97±0.92(+0)	5.12±2.40(+0)
IRAS 02168-0312	167.7551	-57.9827	7.88±3.67(-1)	1.29±0.25(+0)	2.18±0.66(+0)	4.25±2.20(+0)
IRAS 07245+4605	172.2522	+25.2582	1.99±0.36(+0)	3.14±0.32(+0)	5.28±1.12(+0)	1.05±0.42(+1)
IRAS 05528+2010	188.7152	-2.4920	6.39±0.38(+0)	1.56±0.10(+1)	4.10±0.47(+1)	6.49±1.58(+1)
IRAS 03463-0710	195.7116	-43.4296	1.93±0.23(+0)	3.31±0.26(+0)	6.84±1.42(+0)	1.27±0.37(+1)
IRAS 05524+0723	199.7872	-8.9586	7.17±2.46(+0)	1.53±0.16(+1)	3.01±0.41(+1)	4.87±0.74(+1)
IRAS 04020-1551	208.8489	-43.9775	1.18±0.22(+0)	1.56±0.24(+0)	2.80±0.82(+0)	5.98±2.35(+0)
IRAS 03172-2156	212.0889	-55.9956	1.30±0.17(+0)	1.53±0.15(+0)	2.12±0.86(+0)	5.18±1.99(+0)
IRAS 04573-1452	214.3244	-31.3271	1.51±0.22(+0)	2.97±0.24(+0)	7.29±1.35(+0)	1.29±0.42(+1)
IRAS 05251-1244	215.212	-24.2837	2.87±0.37(+0)	7.44±0.84(+0)	1.88±0.26(+1)	3.08±0.54(+1)
IRAS 06176-1036	218.9681	-11.7647	3.09±0.53(+0)	9.49±0.75(+0)	2.91±0.46(+1)	4.94±0.81(+1)
IRAS 09452+1330	221.4465	+45.0603	2.88±0.85(+0)	2.98±0.76(+0)	4.37±1.10(+0)	6.77±2.68(+0)
IRAS 04387-3819	241.3235	-41.3164	7.26±2.66(-1)	9.84±1.45(-1)	2.07±0.45(+0)	6.00±2.30(+0)
IRAS 01246-3248	250.1814	-80.5886	1.32±0.34(+0)	1.65±0.24(+0)	2.48±0.80(+0)	5.03±1.82(+0)
IRAS 05418-4628	252.9465	-30.6841	1.27±0.15(+0)	2.13±0.14(+0)	5.12±1.09(+0)	1.00±0.31(+1)
IRAS 05096-4834	254.8403	-36.2899	6.71±2.11(-1)	9.37±1.39(-1)	1.98±0.58(+0)	4.71±2.43(+0)
IRAS 09429-2148	255.7954	+23.3526	1.54±0.24(+0)	2.49±0.18(+0)	4.32±0.97(+0)	8.47±3.07(+0)
Y Hya	257.5954	+23.5763	1.32±0.26(+0)	2.17±0.19(+0)	4.00±0.79(+0)	7.69±2.20(+0)
IRAS 10350-1307	259.9664	+38.0741	1.70±0.38(+0)	2.54±0.27(+0)	4.18±0.92(+0)	7.86±1.67(+0)
IRAS 10223-1823	261.0509	+32.0499	2.88±0.43(+0)	4.35±0.42(+0)	5.62±1.68(+0)	1.15±0.33(+1)
IRAS 02522-5005	265.4512	-57.3755	9.09±3.21(-1)	1.36±0.19(+0)	2.83±0.85(+0)	6.71±2.63(+0)
IRAS 07059-5818	268.876	-20.9187	1.61±0.27(+0)	3.72±0.20(+0)	8.70±1.88(+0)	1.61±0.34(+1)
IRAS 10580-1803	269.2695	+37.1958	1.84±0.35(+0)	2.42±0.28(+0)	3.59±1.00(+0)	6.09±1.98(+0)
IRAS 04361-6210	272.6714	-39.3424	1.83±0.63(+0)	2.07±0.33(+0)	3.68±0.97(+0)	9.08±3.00(+0)
IRAS 05071-6327	273.2537	-35.6061	1.29±0.25(+0)	1.48±0.14(+0)	2.80±0.73(+0)	6.60±2.60(+0)
IRAS 03112-5730	273.2962	-50.9036	1.08±0.40(+0)	1.26±0.28(+0)	2.40±0.74(+0)	5.26±2.28(+0)
IRAS 02427-5430	273.4748	-55.8918	1.16±0.33(+0)	1.88±0.19(+0)	3.87±1.10(+0)	7.88±2.98(+0)
IRAS 04330-6307	273.9899	-39.4094	1.60±0.40(+0)	1.90±0.27(+0)	3.49±0.89(+0)	8.50±2.82(+0)
IRAS 08349-5945	275.626	-11.4322	2.98±0.29(+0)	7.63±0.46(+0)	1.86±0.26(+1)	3.12±0.59(+1)
IRAS 10329-3918	276.2243	+16.1420	1.71±0.29(+0)	2.95±0.22(+0)	6.79±1.29(+0)	1.26±0.24(+1)
IRAS 09200-5805	278.1592	-5.9364	6.25±0.48(+0)	1.52±0.11(+1)	3.30±0.49(+1)	5.65±1.02(+1)
IRAS 02464-5915	278.8165	-52.2858	1.47±0.41(+0)	1.89±0.44(+0)	2.97±0.83(+0)	6.48±2.81(+0)
IRAS 10323-4611	279.7474	+10.1583	2.59±0.35(+0)	7.18±0.44(+0)	1.63±0.23(+1)	2.74±0.79(+1)
IRAS 11461-3542	288.9348	+25.1725	2.27±0.29(+0)	4.35±0.39(+0)	8.35±1.33(+0)	1.47±0.34(+1)
IRAS 11385-5517	293.0277	+5.9372	7.99±0.88(+0)	2.00±0.17(+1)	3.66±0.36(+1)	5.60±1.31(+1)
IRAS 05411-8625	299.1074	-28.3902	1.97±0.35(+0)	3.86±0.26(+0)	9.24±1.30(+0)	1.82±0.31(+1)
IRAS 14003-7633	307.2199	-14.5442	2.87±0.38(+0)	6.84±0.54(+0)	1.61±0.23(+1)	2.51±0.58(+1)
IRAS 22145-8041	310.0353	-34.4970	1.34±0.27(+0)	3.04±0.14(+0)	8.59±1.75(+0)	1.71±0.45(+1)
IRAS 13001+0527	310.3571	+67.8959	2.01±0.30(+0)	2.33±0.19(+0)	2.65±1.15(+0)	4.47±2.56(+0)
IRAS 15094-6953	314.6046	-10.5162	2.75±0.28(+0)	5.81±0.30(+0)	1.16±0.16(+1)	1.87±0.63(+1)
IRAS F13370-3123	314.86	+30.1061	2.38±0.33(+0)	3.23±0.30(+0)	4.73±1.04(+0)	8.69±2.99(+0)
IRAS 23564-5651	316.9919	-59.1004	7.74±3.09(-1)	8.42±1.30(-1)	1.56±0.62(+0)	4.22±2.20(+0)
IRAS 13462-2807	318.0224	+32.8108	2.81±0.61(+0)	4.39±0.64(+0)	6.70±1.41(+0)	1.02±0.34(+1)
IRAS 21197-6956	323.1957	-38.2022	1.11±0.34(+0)	1.52±0.19(+0)	3.43±0.77(+0)	8.64±2.22(+0)
IRAS 14591-4438	326.0467	+12.0707	4.09±0.36(+0)	8.87±1.02(+0)	1.70±0.32(+1)	2.65±0.78(+1)
IRAS 17389-5742	334.7225	-14.2607	2.44±0.30(+0)	5.65±0.25(+0)	1.05±0.16(+1)	1.91±0.46(+1)
IRAS 20075-6005	337.1507	-33.2112	1.45±0.40(+0)	2.01±0.26(+0)	3.99±1.12(+0)	6.87±2.36(+0)
IRAS 19575-5930	337.848	-31.9574	1.30±0.38(+0)	1.98±0.15(+0)	4.10±1.05(+0)	8.61±2.71(+0)
IRAS 19510-5919	338.0451	-31.1239	1.65±0.52(+0)	2.72±0.18(+0)	4.75±1.18(+0)	1.01±0.23(+1)
IRAS 00254-3317	342.3607	-82.2294	1.17±0.19(+0)	1.12±0.15(+0)	1.27±0.58(+0)	2.86±1.65(+0)
IRAS 22230-4841	345.8847	-54.7672	7.94±2.67(-1)	1.10±0.15(+0)	1.33±0.57(+0)	2.87±1.97(+0)
IRAS 22396-4708	346.2669	-57.9541	6.32±3.58(-1)	9.17±2.07(-1)	1.83±0.75(+0)	4.68±2.45(+0)
IRAS 19143-5032	347.0453	-24.6903	1.79±0.51(+0)	3.11±0.25(+0)	5.67±1.18(+0)	1.07±0.30(+1)
IRAS 22196-4612	350.2821	-55.1638	7.72±3.02(-1)	1.17±0.24(+0)	2.06±0.67(+0)	4.82±2.05(+0)
IRAS 20120-4433	355.7398	-33.1629	1.86±0.50(+0)	2.42±0.26(+0)	3.71±1.17(+0)	6.61±1.98(+0)
IRAS 00128-3219	358.6701	-80.7505	9.43±2.33(-1)	1.15±0.12(+0)	1.31±0.58(+0)	2.63±2.48(+0)

Note - *: the source boundary adopted from a shorter waveband.

Table 5. Newly Resolved Far-IR Sources Found Near the MLHES Targets

No.	RA(J2000)	DEC(J2000)	N65 (MJy sr ⁻¹)	WIDE-S (MJy sr ⁻¹)	WIDE-L (MJy sr ⁻¹)	N160 (MJy sr ⁻¹)	Associated MLHES Source	Identity
1	1.702569	+43.028147	...	1.11±0.63(-1)	6.96±1.24(-2)	2.45±1.60(-2)	IRAS 00042+4248	Unknown
2	6.816878	-6.597084	9.99±2.11(-2)	1.34±0.14(-1)	1.69±0.08(-1)	1.32±0.19(-1)	IRAS 00245-0652	Unknown
3	48.265166	-57.354368	8.17±0.52(-1)	1.21±0.03(+0)	2.01±0.03(+0)	2.18±0.07(+0)	IRAS 03112-5730	ESO 111-12
4	61.051764	-15.751063	1.99±0.03(+0)	3.35±0.02(+0)	1.74±0.03(+0)	4.25±0.31(-1)	IRAS 04020-1551	Unknown
5	70.165871	-38.176343	2.70±1.27(-2)	3.59±0.78(-2)	3.65±0.70(-2)	9.58±1.84(-2)	IRAS 04387-3819	Unknown
6	77.743444	-48.539302	7.32±2.36(-2)	7.46±1.51(-2)	6.06±0.66(-2)	8.09±2.02(-2)	IRAS 05096-4834	Unknown
7	80.416615	-86.415403	1.60±0.28(-1)	1.45±0.19(-1)	2.05±0.29(-1)	2.41±0.50(-1)	IRAS 05367-8627	IRAS 05367-8627
8	85.772116	-46.429199	6.15±1.07(-2)	1.04±0.07(-1)	10.0±1.06(-2)	6.47±2.83(-2)	IRAS 05418-4628	LEDA 526123
9	112.027330	+45.903738	4.53±0.58(-1)	4.97±0.36(-1)	2.08±0.27(-1)	4.18±0.41(-1)	IRAS 07245+4605	NVSS J192806+455415
10	112.151760	+46.023933	7.04±2.31(-2)	5.62±1.61(-2)	2.40±1.30(-2)	...	IRAS 07245+4605	Unknown
11	156.235920	-18.680481	3.46±1.59(-1)	3.96±1.43(-1)	4.12±0.19(-1)	1.62±0.30(-1)	IRAS 10223-1823	2MASX J10245656-1840511
12	156.172150	-18.702896	...	1.27±1.10(-1)	1.60±0.14(-1)	8.71±2.24(-2)	IRAS 10223-1823	2MASX J10244108-1842161
13	158.598138	-46.557139	3.41±1.60(-1)	4.30±1.18(-1)	4.98±0.49(-1)	1.96±0.53(-1)	IRAS 10323-4611	Unknown
14	168.742160	+54.963817	1.99±0.20(-1)	1.18±0.22(-1)	6.65±1.16(-2)	1.66±0.35(-1)	IRAS 11119+5517	MCG +09-19-014
15	199.790730	+45.494444	2.28±1.12(-2)	6.34±0.84(-2)	6.86±0.67(-2)	1.31±0.19(-1)	IRAS 13172+4547	2MASX J13190967+4529332
16	207.266370	+39.497685	1.34±0.26(-1)	2.78±0.17(-1)	3.05±0.14(-1)	7.22±0.37(-1)	IRAS 13468+3947	UGC 8736
17	216.096160	+25.787907	...	1.65±1.34(-1)	1.56±0.16(-1)	1.90±0.27(-1)	IRAS 14219+2555	2MASX J14242307+2547173
18	224.445830	+65.905068	2.40±0.27(-1)	2.81±0.15(-1)	5.12±0.18(-1)	9.28±0.46(-1)	IRAS 14567+6607	Unknown
19	224.219270	+65.933355	2.40±0.27(-1)	2.81±0.15(-1)	5.12±0.18(-1)	9.28±0.46(-1)	IRAS 14567+6607	MCG +11-18-017
20	240.707950	+47.225917	2.47±0.03(+0)	2.29±0.02(+0)	3.68±0.03(+0)	5.75±0.32(-1)	IRAS 16011+4722	UGC 10156
21	283.326860	+33.067801	2.40±1.65(-1)	5.07±2.39(-1)	6.13±0.52(-1)	9.14±0.72(-1)	IRAS 18517+3257	IC 1296
22	283.582100	+36.785821	1.62±0.19(-1)	1.76±0.13(-1)	8.75±1.11(-2)	2.17±1.12(-2)	IRAS 18527+3650	IRAS 18525+3643
23	321.103680	-69.709140	1.21±0.03(+0)	2.05±0.04(+0)	1.12±0.03(+0)	8.38±0.57(-1)	IRAS 21197-6956	Unknown
24	326.270180	+73.668948	1.30±0.28(-1)	2.31±0.19(-1)	3.67±0.32(-1)	4.87±0.44(-1)	IRAS 21440+7324	Unknown
25	335.373800	-80.447149	3.86±0.30(-1)	6.25±0.21(-1)	5.35±0.41(-1)	5.00±0.45(-1)	IRAS 22145-8041	6dFGS gJ222128.0-802653
26	336.475330	-48.500234	7.59±1.85(-2)	6.68±1.15(-2)	5.83±0.86(-2)	1.78±0.25(-1)	IRAS 22230-4841	LEDA 486758
27	345.933400	+28.154108	1.74±0.33(-1)	2.13±0.29(-1)	2.80±0.18(-1)	1.74±0.24(-1)	IRAS 23013+2748	Unknown
28	350.013690	+26.216799	5.65±0.47(-1)	8.39±0.33(-1)	6.44±0.28(-1)	5.94±0.42(-1)	IRAS 23173+2600	Mrk 322